Compact Source for polarization entangled Photon Pairs

Master's Thesis at Max-Plank-Institute for Quantum Optics

Yousef Nazirizadeh

July 31, 2005

Supervisor: Prof. Dr. Harald Weinfurter
Examiner: Prof. Dr. Anders Karlsson

Contents

Chapter 1

Introduction

When about more than 100 year ago Max Planck presented his new idea about the black body radiation, a new physical field was born - the *quantum theory*. Although he was forced to use this kind of thinking to be able to explain the observed result mathematically, this was a prized step for mankind. His idea triggered a whole community which developed the theoretical part of quantum mechanics. From this time on the way of treating the microscopic world was not comparable at all with the classical physics. Phenomena like wave-particle duality or the principle of superposition could not be described in classical physics.

But exactly these phenomena are the one which has the most contribution to nowadays achievement in yielding direct applications of this theory.

Quantum Information is one of the most promising applications of quantum mechanics. It deals with the well known information theory with an additional quantum mechanical aspect. A central role is given to a phenomenon which was described first by Einstein, Podolsky and Rosen [1] and was later called *entanglement* by Schroedinger. In experiments like quantum dense coding [2], teleportation [3] or quantum cryptography [4], which where important milestones in quantum information, entanglement plays the main role.

In this thesis it was our main aim to present a compact and robust source for polarization entangled photons pairs. In the past different methods like using two type-I down-conversion crystals [5], resonant enhancement techniques [6] or using periodically poled crystals [7] have been developed to improve sources in the sense of their efficiency, robustness and size. We focus our work on building a source using spontaneous parametric down-conversion type-II in a non-linear geometry.

This thesis is arranged in the following way. After a historical and physical background for further understanding of the thesis in chapter 2 I will present the theoretical tools which are necessary for the experimental part in chapter 3. The three setups which are experimentally realized are shown in chapter 4. An additional proposal on a new source using a two type-I down-conversion crystals is presented in chapter 5.

Chapter 2

Historical and Physical Background

Entanglement plays a central role in this thesis. The first article dealing with this problem was published in May 1935 by Albert Einstein, Boris Podolsky and Nathan Rosen [1], wherein the authors claim that the description of the physical reality by a quantum mechanical wave function is incomplete. I will introduce their *Gedankenexperiment* and discuss its consequences. About 30 years later John Bell could describe with some modification of this *Gedankenexperiment* an experiment where it was possible to make a step towards the answer of the completeness of quantum mechanics. His idea is still today a measure for the quality of entanglement.

Quantum phenomena like entanglement can be used in modern computation and communication schemes and can improve nowadays capacities. This field is known as *Quantum Information*. I will discuss basic concepts of Quantum Information where we will see that to be flexible in experimental realizations a compact and stable source for polarization entangled photons is beneficial.

As today the most efficient way, of generating entangled photons is spontaneous parametric downconversion, the physical description of it is given later on.

2.1 EPR Pairs

During the development period of quantum mechanics there were many doubts about the logical foundations. This doubts where illustrated in a pronouncing way by famous Gedankenexperiments. The two most well known are Schroedinger's Cat and the Einstein Podolsky Rosen (EPR) Paradox. The latter showed up to be very interesting for arguing pro and contra quantum mechanics.

2.1.1 Einstein Podolsky Rosen Paradox

The EPR *Gedankenexperiment* [1] was the answer to Heisenberg's principle of uncertainty which was a prediction of quantum mechanics. It says that it is not possible to determine with arbitrary precision two non commuting variables like momentum and position. But EPR considers the following: Two quantum particles interact in that way that they will have opposite momentum and will be separated. After some

time one can measure the momentum of one of the particles and can make predictions about the other's momentum. By measuring the position of the second particle, one knows the position of its counterpart. So at least both the position and the momentum of a system are known. Considering every physical theory as local and real quantum mechanics could not be complete, as it cannot describe these values.

Inspired by Bohm's reformulation of the EPR into spins of particle John Bell derived his famous "Bell's inequalities" [8]. He derived his inequalities by trying to complete the Quantum theory by the use of hidden parameter which still is local. But quantum mechanic predicts their violation.

2.1.2 Bell's Theorem

Today still Bell's inequalities and more developed versions are used to prove for various entangled states.

In this part I will discuss the most common form of the Bell inequality, the so called CHSH inequality[1] [9], which is very handy to implement in many experiments.

We consider a quantum state, e.g. of two particles A and B which are far away. In figure 2.1 we see such state consisting of two photons with the implemented experiment, photon A is analyzed by a polarization filter[2] and a detector, photon B is analyzed in the same way.

We can think of a correlation coefficient of the measurements on the two photons and define it in the following way

$$E(a,b) = P_{++}(a,b) + P_{--}(a,b) - P_{+-}(a,b) - P_{-+}(a,b) \tag{2.1}$$

with $P_{\pm\pm}(a,b)$ the probability of obtaining the result ± 1 along a on photon A and ± 1 along b on the other photon, where $+1$ is a positive result on the polarization measurement. As we can see in figure 2.1 a and b are the angles of the polarizers.

The CHSH inequality [9] combines the correlation coefficients in the following way

$$S = E(a,b) - E(a,b\prime) + E(a\prime,b) + E(a\prime,b\prime) \tag{2.2}$$

here a and $a\prime$ are two different basis of measurements[3] on one of the particles and b and $b\prime$ are basis of measurements on the other particle.

In classical physics looking at correlated particles S cannot be beyond the following bounds

$$-2 \leq S \leq +2 \tag{2.3}$$

Entanglement how it is predicted by quantum mechanics shows correlation between two particles much stronger than classically possible. With the result of the measurement on one photon we can make predictions about the out coming result of the other

[1] Clauser, Horne, Shimony and Holt inequality

[2] a photon can pass or not pass the filter depending on his polarization and the orientation of the filter

[3] the direction of the polarization filter plus detector is called base of measurement

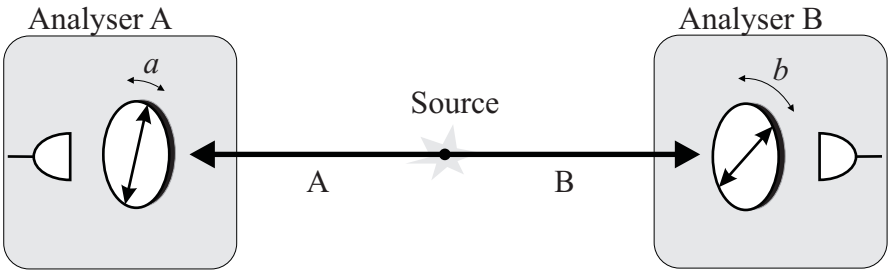

Figure 2.1: *Polarization correlation measurement on photons: the Source emits two photons A and B, these photons are analyzed with two polarizers plus detectors at angles of a and b*

photon. This is possible in any base of measurement. We refer to base of measurement as the direction of the polarization filter plus detector.

If we look at figure 2.1 again and use Malus' Law for an entangled state[4] we get for the probability that two photons pass both polarizers this expression

$$P_{\pm\pm}(a,b) = \frac{1}{2}\cos^2(a-b) \tag{2.4}$$

And on the other hand the probability that only one of the photons passes its filter but not the other one is described by the following

$$P_{\pm\mp}(a,b) = \frac{1}{2}\sin^2(a-b) \tag{2.5}$$

Using equation (2.4) and (2.5) we get the following expression for the correlation coefficient

$$\begin{aligned} E(a,b) &= \frac{1}{2}\cos^2(a-b) + \frac{1}{2}\cos^2(a-b) - \frac{1}{2}\sin^2(a-b) - \frac{1}{2}\sin^2(a-b) \\ &= \cos 2(a-b) \end{aligned} \tag{2.6}$$

By analyzing S (equation 2.2) we can see in figure 2.2 that quantum mechanic predicts the violation of CHSH-inequality for some angles. One set of angles can be $(a-b) = (b-a\prime) = (a\prime - b\prime) = 22.5°$ and $(a-b\prime) = 67.5°$ for this set the value for $S = 2\sqrt{2} > 2$.

After the publication of Bell's inequalities many groups tried to use it to prove that *hidden-variable* theories are incorrect. The first group who could take a big step towards it was Aspect et al. [10] in 1981.

2.2 Principles of Quantum Information

The principle of quantum information is to encode information in a quantum state of a physical system to process and communicate with it. *Entanglement* and *Superposition*

[4] $|\phi^+\rangle$ a maximally entangled state

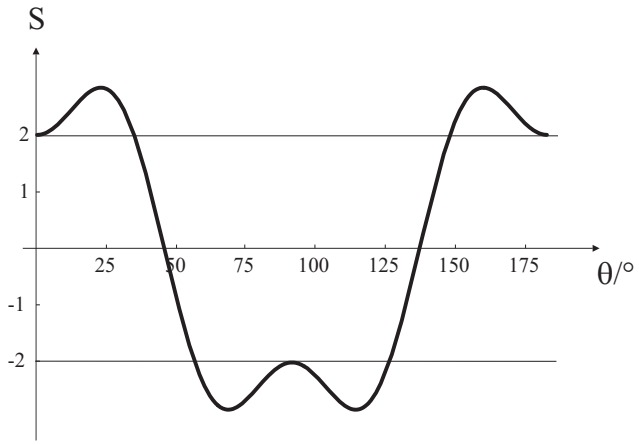

Figure 2.2: *Quantum mechanical prediction on S versus different angles* $\theta = (a - b) = (b - a\prime) = (a\prime - b\prime) = 3(a - b\prime)$*: One can see that* $\theta = 22.5°$ *is one of the angles where the violation has its maximum*

are quantum resources which allow to achieve tasks which are classically impossible. As a physical system one can take the spin of an electron, the two level of an atom or like in our case the polarization of a photon.

2.2.1 One and two Qubit systems

In classical information theory the information carrier is a bit, it can have the value 0 and 1. In contrast to a classical bit in a quantum system there can be encoded not just two states but also a superposition of these two states. The unit in quantum information is the so-called *qubit* (quantum bit). In case of photons these two basis states can be $|H\rangle$ for horizontally polarized photons and $|V\rangle$ for vertically polarized photons. The most general state which represents a qubit is

$$|\psi\rangle = \cos\frac{\theta}{2}|H\rangle + \sin\frac{\theta}{2}e^{i\phi}|V\rangle \tag{2.7}$$

$|H\rangle$ and $|V\rangle$ are orthogonal basis vectors which span a two dimensional Hilbert space.

The Poincaré sphere[5] provides a convenient way of representing polarized light, $|\psi\rangle$ represents a point on this sphere (figure 2.3).

In figure 2.3 the following expressions are used:
$|R\rangle$[6]$=|H\rangle + i|V\rangle$
$|L\rangle$[7]$=|H\rangle - i|V\rangle$
$|+\rangle$[8]$= |H\rangle + |V\rangle$
$|-\rangle$[9]$=|H\rangle - |V\rangle$

[5] a special case of Bloch sphere
[6] Right-hand circular polarization
[7] Left-hand circular polarization
[8] $+45°$ linear polarization
[9] $-45°$ linear polarization

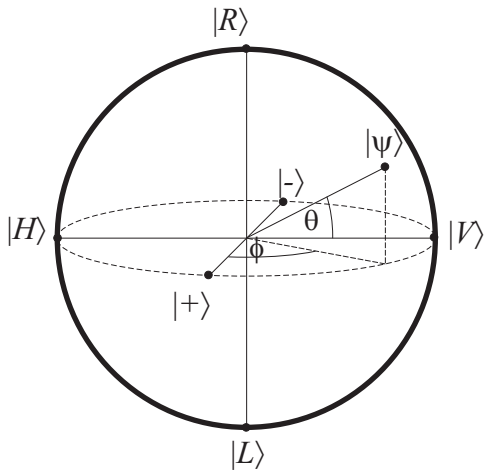

Figure 2.3: *The Pintcaré sphere: representation of the Hilbert space of one qubit*

A two-qubit system on the other hand can be written as a tensor product of two one-qubit systems like $|\phi\rangle \otimes |\phi\prime\rangle$. A special pure state can be create which cannot be written as a tensor product of two one-qubit systems

$$|\psi\rangle_{1,2} \neq |\psi\rangle_1 \otimes |\psi\rangle_2 \tag{2.8}$$

These two-qubit states are called *entangled* states. These states show maximal correlation like discussed in chapter 2.1.1.

Examples for maximally entangled states are the so-called *Bell states*

$$|\phi^+\rangle = \frac{1}{\sqrt{2}}(|HH\rangle + |VV\rangle) \tag{2.9}$$

$$|\phi^-\rangle = \frac{1}{\sqrt{2}}(|HH\rangle - |VV\rangle) \tag{2.10}$$

$$|\psi^+\rangle = \frac{1}{\sqrt{2}}(|HV\rangle + |VH\rangle) \tag{2.11}$$

$$|\psi^+-\rangle = \frac{1}{\sqrt{2}}(|HV\rangle - |VH\rangle) \tag{2.12}$$

By using the quantum mechanical properties of one and multi-qubit systems one can think of many experiments beating classical bounds. The most important ones are presented in the next part.

2.2.2 Experimental achievement

In the last 20 years many experimental proposals towards quantum information were done and in the last 10 year lots of these experiments were realized in lab. We talk about two main field: Quantum *Communication* and *Computation*. The realized experiments however are still basic primitives. I will mention the most popular ones.

Quantum dense coding was proposed by Bennet et al. [2]. With this protocol it is possible to send two bits of classical information by one photon, if the two parties share an entangled photon pair. This experiment was realized in [11].

Quantum teleportation allows to transfer an unknown quantum state from a sender to a receiver. This was proposed by Bennet et al. [3]. Already in 1997 experimental results were published in [12].

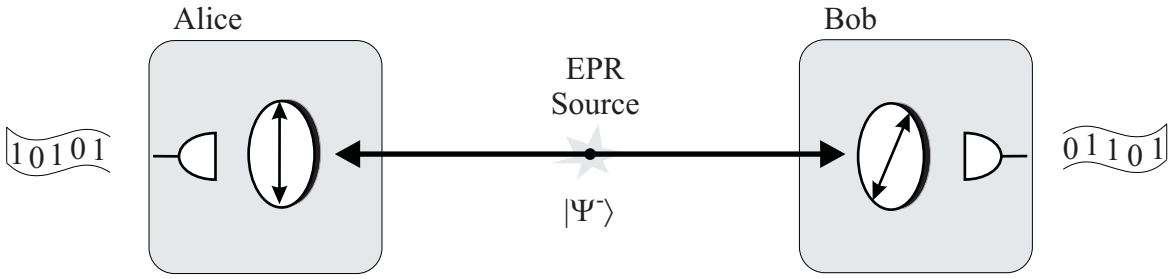

Figure 2.4: *Ekert Protocol: Two entangled photons are distributed to Alice and Bob; they can make polarization measurements in randomly chosen basis and can generate a key for secure communication*

Another experiment which is very successful and has already commercial applications is quantum cryptography. There are many protocols proposed like in 1970 by Wiesner [13] or the BB84 [14]. But the first protocol which used entangled states was the Ekert-Protocol [4]. The Ekert-Protocol is the following: An EPR source distributes entangled photon pairs in one of the Bell states, like $\frac{1}{\sqrt{2}}(|HV\rangle + |VH\rangle)$, which can be also written in another base[10] like $\frac{1}{\sqrt{2}}(|+-\rangle + |-+\rangle)$ between sender Alice and receiver Bob[11] (figure 2.4). Alice and Bob analyze the polarization of each photon in a randomly and independently chosen basis[12] and remember the results. Afterwards the information about the chosen basis is exchanged through a classical link. Due to the entanglement Alice and Bob will see perfect correlation in their results where they chose the same basis. Using this method they can distribute a key to communicate secure. In the cases they chose different basis they can use this data for checking for eavesdropper, they announce these data since it cannot be used for the key and can violate the CHSH-inequality if there was no eavesdropper in the link. The big advantage of this protocol is that it is not necessary to have a trusted source.

2.3 Spontaneous Parametric Down-conversion

For all these experiments a source of entangled photon pairs is required. *Spontaneous Parametric Down-conversion* (SPDC) proofed itself to be a stable and efficient technique for this task [15]. As the sources presented in this thesis rely on that process I will give a physical background about it.

[10] set of polarizers and detectors which analyzes the polarization of the photon
[11] Alice and Bob are notations from the classical cryptography which stands for A and B
[12] HV basis or +- basis

2.3.1 Physical Background

We start with the expansion of the electrical polarization in a crystal:

$$P^i = \epsilon_0(\chi^{(1)}_{ij}E^j + \chi^{(2)}_{ijk}E^jE^k + \chi^{(3)}_{ijkl}E^jE^kE^l + ...) \tag{2.13}$$

where ϵ_0 is the dielectricity and E_i are the electro magnetic fields. The coefficients χ are the susceptibilities and have increasing values for higher order terms with the following magnitude of order: $\chi^{(1)} \approx 1, \chi^{(2)} \approx 10^{-10}, \chi^{(3)} \approx 10^{-17}$.

The first term of equation (2.13) describes the linear response of the crystal like *refraction* and *dispersion*, the second one describes nonlinear effects like *tree-wave-mixing*. In terms of photons the second order term also describes the amplitude of the spontaneous creation of two down-conversion photons (usually denoted as *idler* and *signal* photon) out of the pump laser. The participating photons have to fulfil the following conditions, which can also be interpreted as energy and momentum conservation [16]

$$\nu_p = \nu_s + \nu_i \tag{2.14}$$

$$\overrightarrow{k_p} = \overrightarrow{k_s} + \overrightarrow{k_i} \tag{2.15}$$

where $\nu_{p,i,s}$ is the frequency of the photons and $\overrightarrow{k_{p,i,s}}$ their momentum. From these conditions follows that the created photons are strongly correlated in frequency and direction of emission.

With the help of equations (2.14) and (2.15) one can further show that idler and signal photons of the same frequency are emitted onto the same cone. This will be investigated in more detail in chapter 3.2.

To fulfil the conditions in (2.14) and (2.15) we need to have differences in refractive indices for idler, signal and pump photons. With the help of birefringence crystals where photons with different polarizations have different refractive indices this task can be solved easily. Throughout this thesis we are looking at special kind of this crystals the so called uniaxial crystal, where the refractive indices do not change around a special direction, the optical axis. An ordinary, which beam in such a crystal has a different refractive index than an extraordinary beam, we refer to this refractive indices as n_e and n_o.

We can distinguish two types of SPDC, *type-I* and *-II* according to the polarizations of the pump, idler and signal.

Type I

In SPDC type-I the pump photon has an orthogonal polarization (either ordinary or extraordinary) with respect to idler and signal photons which are equally polarized. Due to the fact that the two photons have the same polarization they will have the same refractive index and thus lie on the same cone.

In figure 2.5 the *degenerate* case is illustrated where the wavelength of both idler and signal are double the pump wavelength. By changing the angle of the pump with

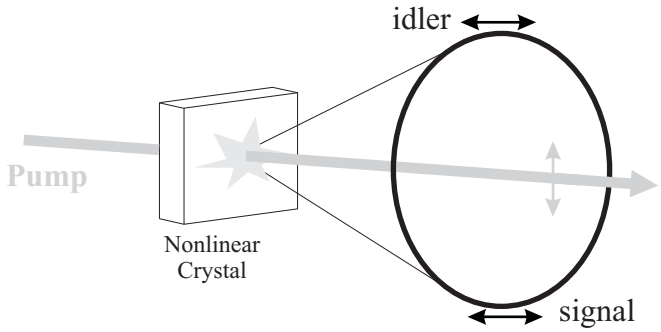

Figure 2.5: *SPDC type-I: degenerate, non-collinear case, idler and signal cone are identical*

respect to the crystal the emission cone changes its size. One can also think of a setting where signal and idler photon are emitted in pump direction, this case is called *collinear* down-conversion. The *Non-collinear* case is demonstrated in figure 2.5.

Type II

In SPDC type-II the idler and signal have orthogonal polarizations (either ordinary or extraordinary). Due to the fact that the refractive indices of the two created photons are different the cones are not coaxial.

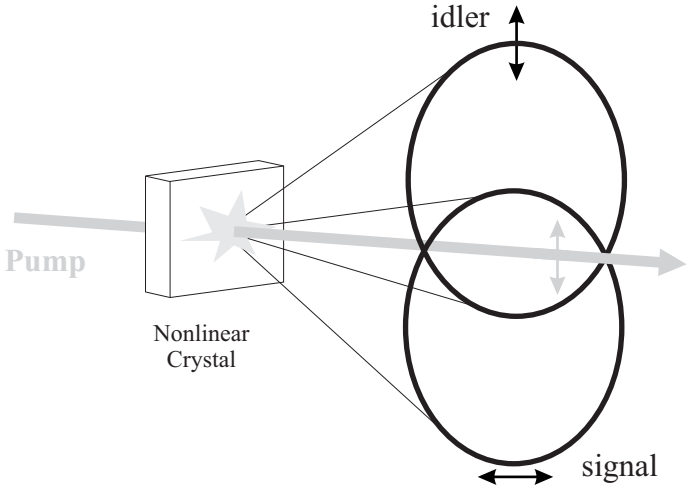

Figure 2.6: *SPDC type-II: degenerate, non-collinear case, idler and signal cones are separated due to different polarization*

Again the size of the cones depends on the angle between pump beam and the optical axis of the crystal. Here the collinear case is, when the two emission cones are tangential. Thus idler and signal can be emitted in pump beam direction.

Detailed calculation about the emission cones in dependence on the experimental parameters are given in chapter 3.2.

2.3.2 Entanglement by Spontaneous Parametric Downconversion

We will discuss how it is possible to generate entanglement with the presented processes. Let me start with SPDC type-II as it is the more simple case.

Say, we use a type-II SPDC source where the idler photons have horizontal (H) and the signal photons vertical (V) polarization. The pump angle is chosen in such a way that the emission cones cross each other. In the crossing points it is not possible to distinguish whether an emitted photon belongs to the idler or to the signal cone. Because of the momentum correlations it is sure that if an idler photon is emitted onto one of the crossing points there is a signal photon emitted onto the other one and vice versa. If we collect photons emitted in these directions, we cannot know the polarization of each photon, just that one is H and the other one V. Therefore one will observe the following state

$$|\psi^+\rangle = \frac{1}{\sqrt{2}}(|HV\rangle + e^{i\phi}|VH\rangle). \tag{2.16}$$

In SPDC type-I there is no natural polarization entanglement as the two emitted photons have the same polarization. With a clever setup, however, like it was realized by Kwiat et al. [5] it is still possible to obtain entanglement. The main idea is to use two crystals whose optical axis are orthogonal. Hence the down-converted photons created in one crystal have orthogonal polarization with respect to the photons created in the other crystal. If we chose the pump polarization in such a way that both crystals are pumped equally and if it is not possible to know where the photons have been created, then we cannot know the polarizations of the photons but that they are equal. The following state is created

$$|\phi^+\rangle = \frac{1}{\sqrt{2}}(|HH\rangle + e^{i\phi}|VV\rangle). \tag{2.17}$$

For both sources the obtained states are Bell states as they were presented in (2.9)-(2.12). It is not important, however, which of the Bell states is generated, as they can be easily transformed into one another.

2.3.3 Walk-Off Effects

In SPDC type-II there are some effects reducing the quality of polarization entanglement, the so-called *walk-off* effects. The different refractive indices for signal and idler photons causes a separation of the idler and the signal beam (*transversal walk-off*) and different group velocities of idler and signal photons (*longitudinal walk-off*). Hence both photons become more distinguishable.

Transversal walk-off

When an extraordinary wave propagates in a birefringent crystal the direction of its $\boldsymbol{k}$ vector does not coincide with the direction of its energy. The angle between these two

vectors is

$$\rho(\theta) = \pm \arctan\left[\left(\frac{n_o(\lambda)}{n_e(\lambda)}\right)^2 \tan\theta\right] \mp \theta \tag{2.18}$$

where θ is the angle between the incident wave and the optical axis, $n_o(\lambda)$ and $n_e(\lambda)$ are the refractive indices of the ordinary and extraordinary waves.

For the ordinary wave, however, the direction of its $\boldsymbol{k}$ vector and the direction of the energy are the same.

Therefore the angle given in equation (2.18) will be observed between a ordinary wave and an extraordinary wave.

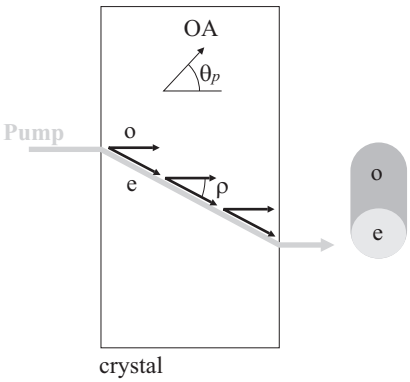

Figure 2.7: *Transversal Walk-Off in a birefringent crystal: the propagation direction of the ordinary (o) and extraordinary (e) waves in a crystal have different directions. Due to down-conversion along the whole crystal the ordinary beam gets an elliptical shape*

The down-conversion happens along the propagation direction of the pump beam through the whole crystal. The angle $\rho(\theta)$ between the ordinary and extraordinary photons separates them. As we can see in figure 2.7 this causes an elliptical shape of the down-converted ordinary beam. The origins of the two ordinary and extraordinary beams are also shifted.

This walk-off increases with the crystal thickness. It can be compensated as will be shown in 4.1.1. If it is, however, significantly smaller than the pump radius it can also be neglected.

Longitudinal walk-off

The longitudinal walk-off occurs due to the fact that the refractive indices of the two created photons is different and therefore they have different group velocities in the crystal. This causes a time delay δt between signal and idler after propagating in crystal. δt is depending on the creation position and is maximum at creation at the first edge of the crystal and is given by the following

$$\delta t_{max} = \frac{\Delta n d}{c} \tag{2.19}$$

where d is the crystal thickness and $\Delta n = |n_o(\lambda) - n_e(\lambda, \theta)|$.

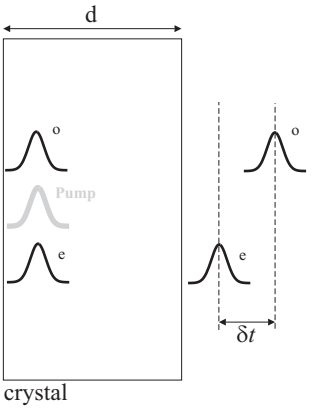

Figure 2.8: *Longitudinal Walk-Off in a birefringence crystal: different group velocities of ordinary (o) and extraordinary (e) waves in the crystal result in a time delay δt between the photons*

If δt_{max} is bigger than the coherence time τ_c of the down-converted photons it allows to distinguish between the signal and the idler photon, which means the loss of entanglement. Again compensation is possible which we will discuss in 4.1.1.

Chapter 3

Theoretical Preparation

The intention of this chapter is to give an overview about all theoretical tools which were used for the design of the compact source. The source can be divided in three main parts, which can be treated separately. The optical pumping of the crystal, the spontaneous nonlinear process in the crystal and the collecting part. A nonlinear crystal is pumped with a coherent light source, a laser beam. Due to the nonlinearity of the crystal a small part of the pump photons are down-converted. Photon pairs are created, whereas the energy conservation is fulfilled. These photons, created under a defined angle, are fitted to a gaussian mode provided by a single-mode fibre to collect them.

Starting with a pump beam we need to introduce gaussian optics since this is a good approximation for a laser beam. I will briefly introduce the parameters of a gaussian beam which are important for further understanding. It is also shown how to deal with the M^2-Factor, which is an important parameter for a real laser beam. It is also used for further calculations like the transformation of the beam by lenses. In some parts of the design it makes more sense to use ray-tracing, for example if we consider that the down-converted photons have a very short coherence length, in this case ray optics is a nice solution.

To have an overview about the emission directions of the down-converted photon pairs I will solve in detail the momentum and energy conservation equations for uniaxial crystals. One of the basic steps is to have a well defined coordinate system and variables which gives the right environment for the calculations. Aiming for warranted results in this calculations many aspects are taken into account like the refraction of both the pump beam and the down-converted photons at the surfaces of the crystal or the free space propagation using ray-tracing. From this results we know with a defined real beam how the cones of the downconversion either for type I or type II would look like. This allows us to optimize for several setting of the source. I will present some calculated cases.

At the end of this chapter I will also describe the idea of mode matching which is an important part of the design which gives some settings of the source. From this result one can generate the crystal thickness, it can be chosen in that way that it is optimized to the coupling mode.

3.1 Linear Optics

3.1.1 Gaussian Optics

To describe a beam we start from a paraxial solution of the Helmholtz equation. For the complex field amplitude of a beam we have the following expression

$$U(\mathbf{r}) = A_0 \frac{w_0}{w(z)} \exp\Big[-\frac{\rho^2}{w^2(z)}\Big] \exp\Big[-jkz - jk\frac{\rho^2}{2R(z)} + j\zeta(z)\Big] \tag{3.1}$$

where $\mathbf{r}$ is the position ($\mathbf{r} = (x, y, z)$) and $\rho = (x^2 + y^2)^{1/2}$ the radial distance to the center of the beam and z is the propagation direction. In equation (3.1) the following beam parameters are introduced

$$w(z) = w_0\Big[1 + \Big(\frac{z}{z_0}\Big)^2\Big]^{1/2} \tag{3.2}$$

$$R(z) = z\Big[1 + \Big(\frac{z_0}{z}\Big)^2\Big] \tag{3.3}$$

$$\zeta(z) = \arctan\Big(\frac{z}{z_0}\Big) \tag{3.4}$$

$$w_0 = \Big(\frac{\lambda z_0}{\pi}\Big)^{1/2} \tag{3.5}$$

there $w(z)$ determines the distance ρ at which the field amplitude is reduced by a factor of $1/e$ in respect to its axial value at $\rho = 0$. We will refer to this parameter as the *beam radius*. The parameter w_0 is the beam radius at $z = 0$ and is called *waist size*. $R(z)$ is the radius of the curvature of the wave front at the distance z. z_0 is defined as the *Rayleigth length*, this gives an approximation about the depth of the focus.

We refer to equation (3.1) as the fundamental gaussian beam, this solution is also called the TM_{00} mode. To follow the whole derivation one can use [17] or [18].

By following the derivation of equation (3.1) one can see that q describes all properties of a gaussian beam

$$\frac{1}{q(z)} = \frac{1}{R(z)} - j\frac{\lambda}{\pi w^2(z)} \tag{3.6}$$

Gaussian Beam properties

Many interesting beam parameters can be derived from equation (3.2) to (3.5) and are discussed in the following.

The optical intensity is given by the square of the absolute value of complex field amplitude introduced in equation (3.1)

$$I(\rho, z) = I_0\Big[\frac{w_0}{w(z)}\Big]^2 \exp\Big[-\frac{2\rho^2}{w^2(z)}\Big] \tag{3.7}$$

From this formula we can calculate the intensity distribution of a gaussian beam at any distance z (figure 3.1(a)). By looking more close to equation (3.7) and (figure

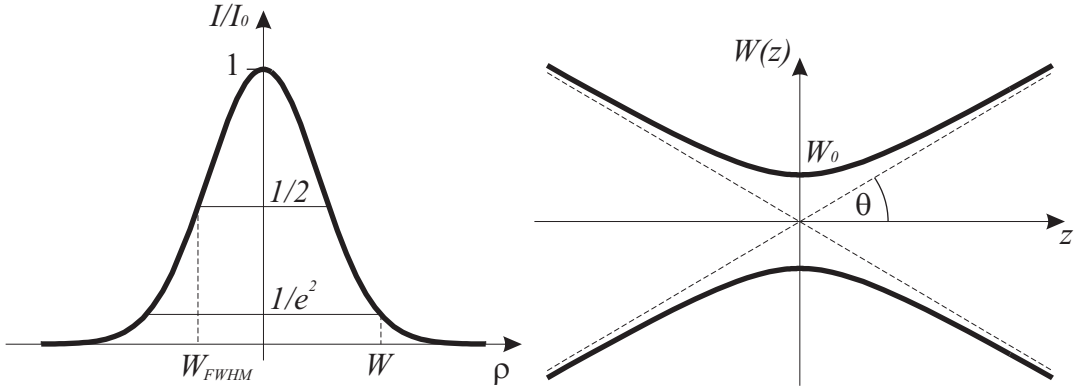

(a) *Normalized Beam intensity: one can see the typical gaussian distribution and the definition of* w_0 *and* W_{FWHM}

(b) *Beam radius* $w(z)$*: We see* w_0 *at* $z = 0$

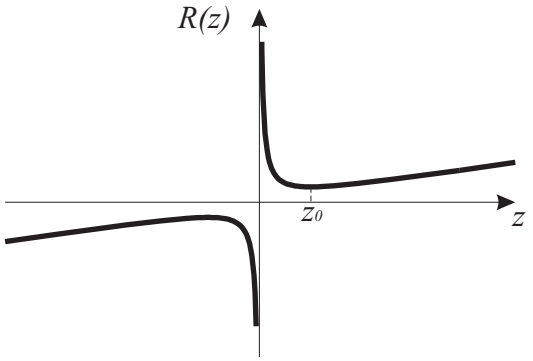

(c) *Radius of beam curvature* $R(z)$*: minimum at* $z = z_0$

Figure 3.1: *Gaussian beam profiles*

3.1(a)) we will see the gaussian behavior, which gives the name *Gaussian optics*. We define also the $w_{FWHM}(z)$[1] which is the diameter of the beam where the intensity is half of the maximum intensity.

To investigate how the beam radius behaves in z-direction we can plot $w(z)$ according to (3.2) and will see that if we are far enough from the center of the beam the beam radius grows linearly (figure 3.1(b)). This happens for z bigger than the Rayleigh length z_0. The angle of the beam radius is then

$$\theta = \frac{\lambda}{\pi w_0} \tag{3.8}$$

We refer to this angle as the *divergence* of the beam.

At $z = z_0$ the curvature of the wavefront decreases to its minimum value. This we see if we plot the wavefront curvature $R(z)$ introduced in (3.3). We also see that $R(0)$ is infinite, this means that at $z = 0$ we have a plane wavefront.

To define and work with a theoretical gaussian beam the wavelength and the waist

[1]FWHM stands for Full Width at Half Maximum

size are sufficient parameters. In case of a real beam, however, we have to deal with an additional parameter, namely the M^2-Factor.

M²-Factor

Unfortunately a real-life laser does not provide true zero order gaussian mode, but also higher order modes. To have a measure for it the M^2-Factor is introduced. The M^2-Factor[2] defines a value which characterizes the differences between an theoretical gaussian beam like defined in equation (3.1) and a real beam. The diameter of the real beam at every distance is M times larger than the diameter of the theoretical gaussian beam [19]

$$w_{REAL}(z) = w(z)M \tag{3.9}$$

From equation (3.9) and (3.2, 3.5) we can derive the parameter which are interesting for us like

$$w_{REAL}(z) = w_0\Big[1 + \Big(\frac{z\lambda M^2}{\pi w_0^2}\Big)^2\Big]^{1/2} \tag{3.10}$$

$$\theta_{REAL} = \lambda\frac{M^2}{w_0\pi} \tag{3.11}$$

One of the ways to determine the M^2 experimentally is by measuring the beam radius at different distances. Equation (3.10) can be fitted to the measured data and one can estimate the M^2. As we will see a real beam may also have different M^2 in horizontal and vertical planes. Also other beam asymmetries can be observed like *Astigmatism* and *Asymmetric Waist* [19]. Astigmatism means that the waist do not have the same position, whereas different sizes of waist is called by Asymmetric Waist.

Once the M^2-factor is known one can analytically describe the propagation of the beam through any optical system. This issue is addressed in the next section.

Gaussian Transformation

By passing an optical system like a lens the parameters of a gaussian beam, like the waist size and waist position, are generally changed. We will refer to this fact as *gaussian transformation*.

One of the most common ways to describe a gaussian transformation is by using the ABCD law. The advantage of this method is that the same matrices as used as in matrix optics, which are introduced in the next section. The transformation is done on the q-parameter of the incident beam

$$q_2 = \frac{Aq_1 + B}{Cq_1 + D}, \tag{3.12}$$

where q_1 is the incident gaussian beam defined like equation (3.6) and q_2 is the transmitted gaussian beam.

[2] real beam $M^2 \geq 1$, perfect gaussian beam $M^2 = 1$

3.1.2 Raytracing

Raytracing via matrix optics is one of the most general ways to treat paraxial rays[3]. Each ray is described by its radial position a and its angle α relative to the optical axis. These variables change by passing an optical system due to Snell's law or geometries.The new position $a\prime$ and angle $\alpha\prime$ are determined using the following transformation

$$\begin{pmatrix} a\prime \\ \alpha\prime \end{pmatrix} = M \begin{pmatrix} a \\ \alpha \end{pmatrix} \tag{3.13}$$

where M is a $2x2$ *ray transfer matrix* with elements A,B,C and D which uniquely characterizes any optical element. In case of a ray passing free space the transfer matrix is the following

$$\begin{pmatrix} 1 & d \\ 0 & 1 \end{pmatrix}, \tag{3.14}$$

where d is the free space length. The matrix for a lens looks the following

$$\begin{pmatrix} 1 & 0 \\ \frac{-1}{f} & 1 \end{pmatrix}, \tag{3.15}$$

where f is the focal length of the lens.

The transfer matrix of a composed system consisting of more than one component is calculated by multiplying all the transfer matrices of each component.

3.2 Phase-Matching for SPDC

This chapter contains the detailed description of the down-conversion process, which are necessary for the design of the setup. We handle this task by solving the *phase matching* conditions, which are the energy and momentum conservation conditions introduced in chapter 2.3

$$\nu_p = \nu_s + \nu_i \tag{3.16}$$

$$\overrightarrow{k}_p = \overrightarrow{k}_s + \overrightarrow{k}_i \tag{3.17}$$

where the indices p, i and s stand for pump, signal and idler. Applying further conditions, which depend on geometry of nonlinear process and type of phase matching, one can derive one single formula. After introducing the refractive indices in the crystal and defining a general coordinate system it is possible to solve this formula. This solutions can be angular or wavelength distributions.

We restrict ourself to the case of uniaxial crystals, but otherwise our calculations keep their generality, so that one can study many cases, collinear or non-collinear, pairs of down-converted photons with or without equal frequencies.

[3]rays propagating under a small angle (such that $sin\theta) \approx \theta$) with respect to optical angle are called paraxial rays

Due to the complexity of some of the setups it was in our interest to simulate how a real laser beam would be down-converted. For this purpose we superposed single results and estimate the real shape of the down-conversion.

3.2.1 Refractive Indices in Uniaxial Crystals

As $k = \frac{\omega n(\lambda,\theta)}{c}$ we need to investigate the refractive index in nonlinear crystals. In this section we concentrate on this issue.

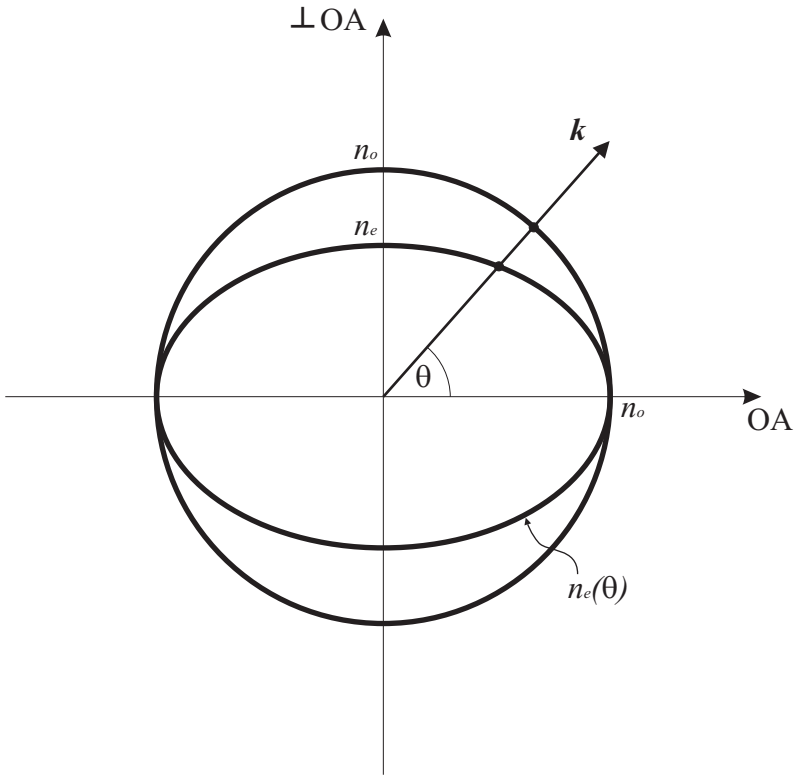

Figure 3.2: *The refractive index of light in a negative uniaxial crystal: the refractive index of a beam depending on the polarization is given at the intersection point between the* $\boldsymbol{k}$ *vector and the curve*

In uniaxial[4] crystals there exists a special direction which is called the Optic Axis (OA). If the polarization of a wave lies in the plane of the OA and its $\boldsymbol{k}$ vector, it is called *extraordinary* (e) wave and if the polarization is normal to this plane it is called *ordinary* (o) wave. The refractive index of the ordinary beam is independent of the angle between its $\boldsymbol{k}$ vector and the OA. For the extraordinary beam the refractive index changes with the angle between $\boldsymbol{k}$ and OA (figure 3.2).

Because of the fact that we are later using *negative uniaxial* crystals figure (3.2) shows an negative uniaxial crystal. In negative crystals n_o has a higher value than n_e[5].

[4]there exist also biaxial crystals which have not just one OA but two

[5]in positive uniaxial crystals $n_o < n_e$

The intersection point between the k and the corresponding curve defines the refractive index.

n_o and n_e are constant values for each crystal at a certain wavelength. The dependence on λ can be expressed by the Sellmeier equation

$$n^2_{o/e}(\lambda) = 1 + \frac{B_1\lambda^2}{\lambda^2 - C_1} + \frac{B_2\lambda^2}{\lambda^2 - C_2} + \frac{B_3\lambda^2}{\lambda^2 - C_3} \tag{3.18}$$

where $B_{1,2,3}$ and $C_{1,2,3}$ are the Sellmeier coefficients, which are found for every material experimentally. For common nonlinear crystals they can be found in [20].

In figure 3.3 we can see the ellipsoid behavior of the refractive index for the extraordinary beam. The refractive index is given at the intersection point of the $\boldsymbol{k}$ vector of the beam with the ellipsoid. Due to rotational symmetry it is just depending on the angle θ.

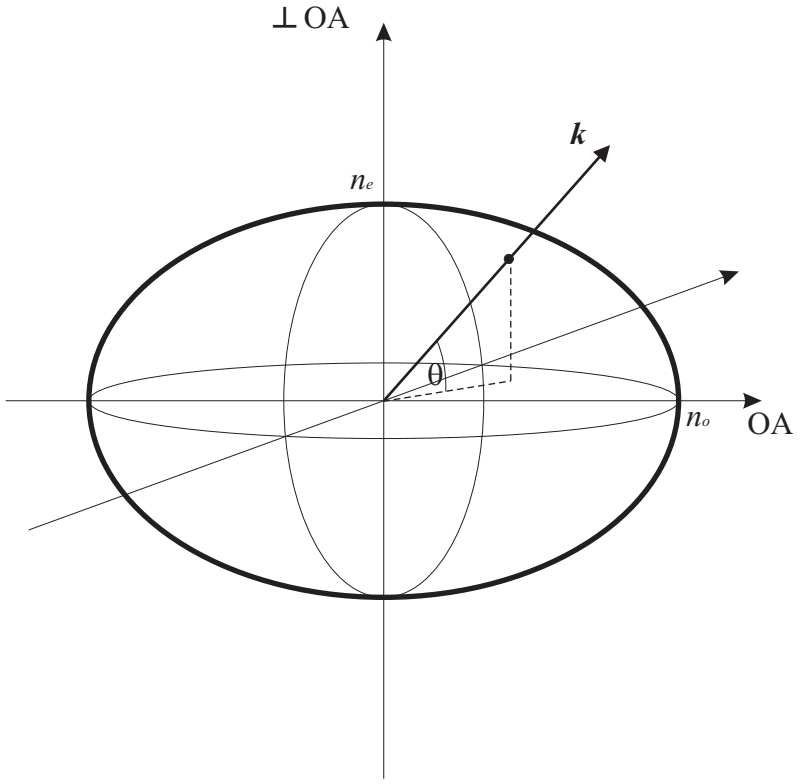

Figure 3.3: *The refractive index of an extraordinary beam in a uniaxial crystal: The intersection point between* $\boldsymbol{k}$ *and the ellipsoid defines the refractive index*

By knowing the angle θ and using the formula for an ellipse

$$\frac{1}{n^2_e(\lambda,\theta)} = \frac{\cos^2(\theta)}{n^2_o(\lambda)} + \frac{\sin^2(\theta)}{n^2_e(\lambda)}, \tag{3.19}$$

we can derive the equation for the refractive index of an extraordinary beam depending on θ:

$$n_e(\lambda,\theta) = \frac{n_o^2(\lambda)n_e^2(\lambda)}{\sqrt{n_o^2(\lambda) + (n_e^2(\lambda) - n_o^2(\lambda))\cos^2(\theta)}}. \tag{3.20}$$

3.2.2 Definition of Coordinate system and Variables

As a necessary prerequisite to solve the phase-matching conditions, it is important to establish a suitable environment, normally a coordinate system with variables. We will use a cartesian coordinate system where one of the axis is identical to the optic axis of a nonlinear crystal (figure 3.4). For calculation this choice is beneficial because the reflective index is defined by the angle of beam of interest with the OA. For better clarity only the idler vector is displayed in figure 3.4, the signal vector is defined exactly the same way but with different notations.

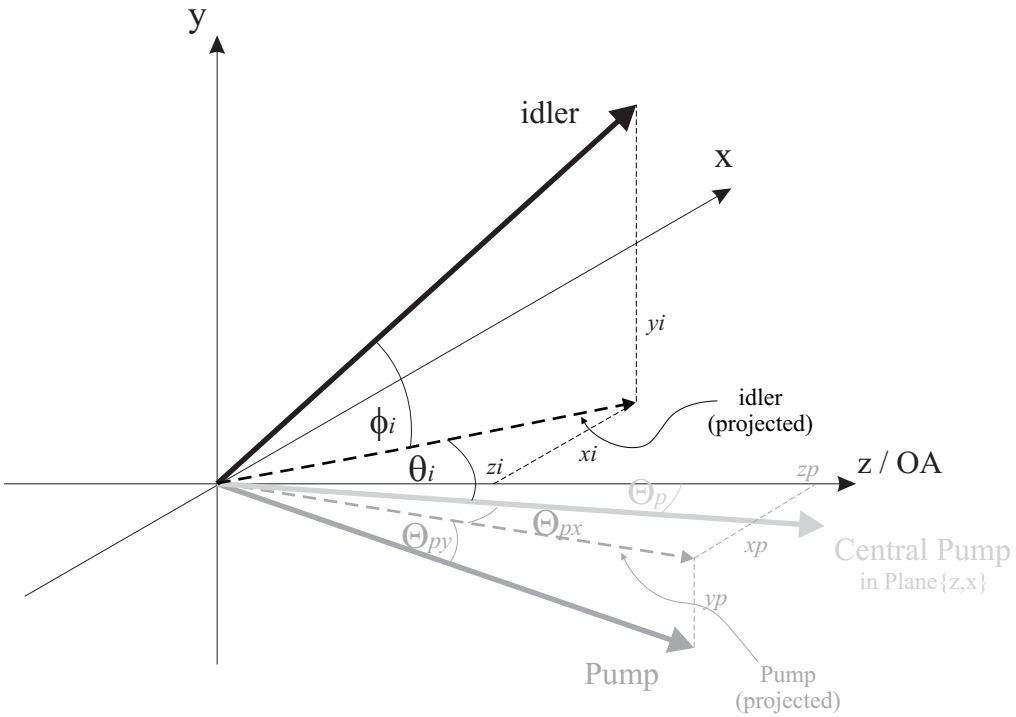

Figure 3.4: *Coordinate system for phase matching*

In figure 3.4 we can see three main vectors: idler, pump and central pump. The idler vector is given by the angles θ_i and ϕ_i which are defined relative to the central pump beam.

For some of the calculations we want to solve the phase-matching conditions for an array of pump directions to simulate a gaussian beam. This is the reason why we introduce the two pump vectors in figure 3.4 , namely pump and central pump. The Pump vector is the actual pump direction, where the Central Pump vector display the origin of the gaussian beam. In calculations where we assume just one pump direction the Pump vector is the same as central pump, i.e. Θ_{px} and Θ_{py} are equal to zero.

From figure 3.4 and the normalization of idler and pump vectors to **1** we find the dependencies of $y_{i,p}$ and $z_{i,p}$ on $\Theta_{p,px,py}$, θ_i and ϕ_i. we will need this to express the momentum conservation

$$y_i = \sin(\phi_i) \tag{3.21}$$

$$z_i = \cos(\Theta_p - \theta_i)\sqrt{1 - y_i^2} \tag{3.22}$$

$$y_p = \sin(\Theta_{py}) \tag{3.23}$$

$$z_p = \cos(\Theta_p + \Theta_{px})\sqrt{1 - y_p^2} \tag{3.24}$$

As the phase-matching holds only inside the crystal and we are interested in the angular distribution outside crystal we need to deal with the refractions of all beams on the crystal surfaces. We introduce the angles between the central pump vector and the the normal to the surface, this allows us to keep the central pump vector as the origin of the setup. This angle is different inside and outside crystal. Figure 3.5 demonstrates the definitions of α_{in} and α_{out}.

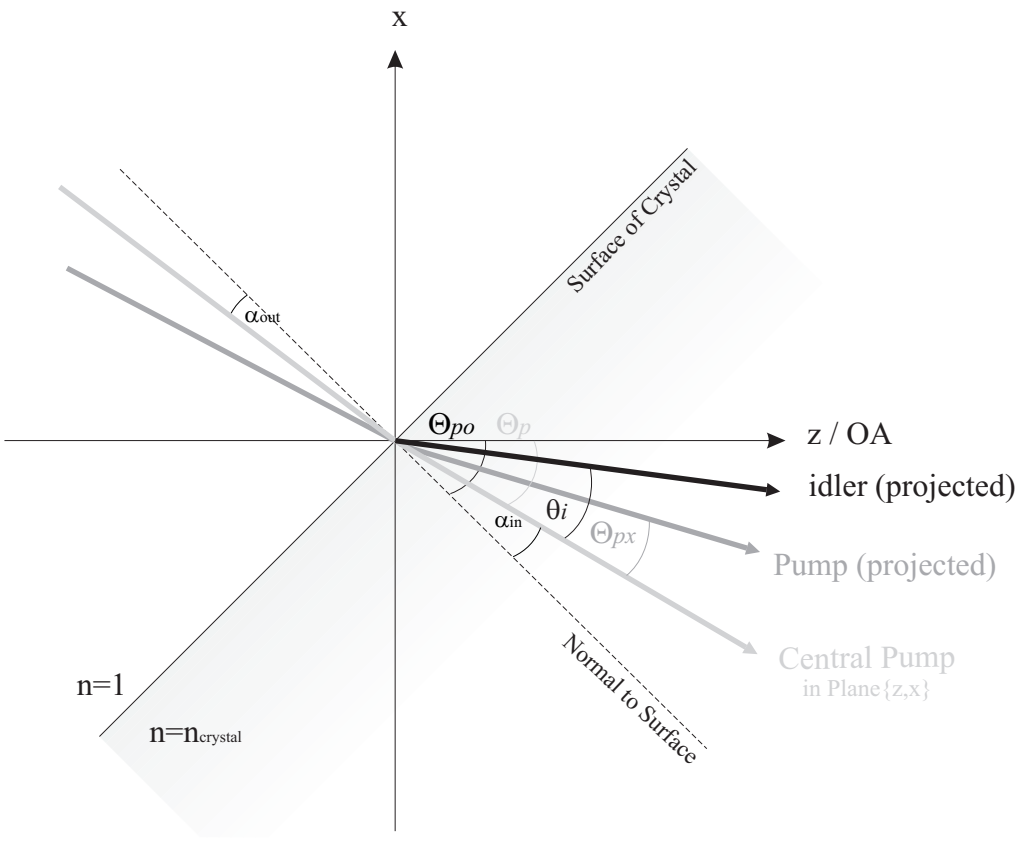

Figure 3.5: *Definition of angel transformation on the crystal surface*

One physical parameter which is given by the crystal is Θ_{po}, this angel is defined by the cut of the crystal, it is the angel between the OA and the normal to the surface.

We define α_{out} according to Snell's law the following way

$$\alpha_{out} = \arcsin(n(\theta_p, \lambda_p) \sin(\alpha_{in})) \tag{3.25}$$

and

$$\beta = \Theta_{po} - \Theta_p \tag{3.26}$$

After this fundamental definitions we can start to discuss the phase-matching itself.

3.2.3 Formula for various Phase-Matching Conditions

The down-conversion occurs just under certain conditions, the so called phase-matching conditions. These conditions are put in the environment which we defined before. As shown in chapter 2.3 there exist two types of down-conversion, type I and II. For each of these cases we will derive, in the next part, a single formula.

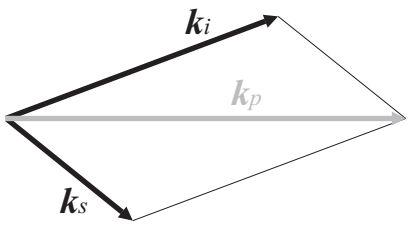

Figure 3.6: *Momentum conservation in a non-collinear case*

Type I

The down-conversion is called type-I if the down-converted photons have the same polarization, but perpendicular with respect to pump photons. In our case we will pump our crystal with extraordinary polarized pump beam and will observe ordinary polarized signal and idler photons. Therefore I derive the formula fitting to this application. The following calculations are made for the idler beam, once we calculated the vector for the idler photons it is very easy to calculate from this the vector of the signal photon.

With $k = \frac{\omega n}{c}$ and equation (2.15) and the notations introduced in chapter 3.2.2, we obtain the following expressions

$$\omega_s n_{os}(\lambda_s) x_s + \omega_i n_{oi}(\lambda_i) x_i = \omega_p n_{ep}(\lambda_p, \theta_p) x_p \tag{3.27}$$

$$\omega_s n_{os}(\lambda_s) y_s + \omega_i n_{oi}(\lambda_i) y_i = \omega_p n_{ep}(\lambda_p, \theta_p) y_p \tag{3.28}$$

$$\omega_s n_{os}(\lambda_s) z_s + \omega_i n_{oi}(\lambda_i) z_i = \omega_p n_{ep}(\lambda_p, \theta_p) z_p \tag{3.29}$$

here already the properties of the downconversion type I are included, in that way that the refractive indices of the idler and signal photons are for ordinary beams.

The linear set of equations (3.27-3.29) is solved with regard to signal cartesian components x_s, y_s and z_s. Taking equation (2.14) into account we obtain the following

$$x_s = \frac{-n_{oi}(\lambda_i)\omega_p x_i + n_{oi}(\lambda_i)\omega_s x_i + n_{ep}(\lambda_p,\theta_p)\omega_p x_p}{n_{os}(\lambda_s)\omega_s} \tag{3.30}$$

$$y_s = \frac{-n_{oi}(\lambda_i)\omega_p y_i + n_{oi}(\lambda_i)\omega_s y_i + n_{ep}(\lambda_p,\theta_p)\omega_p y_p}{n_{os}(\lambda_s)\omega_s} \tag{3.31}$$

$$z_s = \frac{-n_{oi}(\lambda_i)\omega_p z_i + n_{oi}(\lambda_i)\omega_s z_i + n_{ep}(\lambda_p,\theta_p)\omega_p z_p}{n_{os}(\lambda_s)\omega_s} \tag{3.32}$$

For simplicity we do not work in real space, but in momentum space (also known as k-space), where only directions of vectors are of interest. Therefore we normalize the length of all vectors to 1 without any loss of generality. We normalize the signal vector with $x_s^2 + y_s^2 + z_s^2 = 1$. And with $\omega_s = \omega_p - \omega_i$ we get

$$\begin{aligned} &((-n_{oi}(\lambda_i)\omega_i x_i + n_{ep}(\lambda_p,\theta_p)\omega_p x_p)^2 \\ &+(-n_{oi}(\lambda_i)\omega_i y_i + n_{ep}(\lambda_p,\theta_p)\omega_p y_p)^2 \\ &+(-n_{oi}(\lambda_i)\omega_i z_i + n_{ep}(\lambda_p,\theta_p)\omega_p z_p)^2) \quad &= \quad n_{os}^2(\lambda_s)(-\omega_i + \omega_p)^2 \end{aligned} \tag{3.33}$$

with the final normalization of pump and idler vectors we get

$$\begin{aligned} &(n_{ep}(\lambda_p,\theta_p)\omega_p y_p - n_{oi}(\lambda_i)\omega_i y_i)^2 + (n_{ep}(\lambda_p,\theta_p)\omega_p z_p - n_{oi}(\lambda_i)\omega_i z_i)^2 \\ &\quad +(n_{ep}(\lambda_p,\theta_p)\omega_p\sqrt{1-y_p^2-z_p^2} - n_{oi}(\lambda_i)\omega_i\sqrt{1-y_i^2-z_i^2})^2 \quad &= \quad n_{os}^2(\lambda_s)(\omega_p-\omega_i)^2 \end{aligned} \tag{3.34}$$

Assuming certain $\overrightarrow{k}_p$ vector of pump and certain nonlinear crystal equation (3.34) can be solved numerically to find emission directions of idler photons inside the crystal. Corresponding signal vectors can be obtained by applying formulas (3.30 - 3.32).

Type II

In down-conversion type-II the idler and signal photons have orthogonal polarization. The case which we are going to look at, the pump and the idler beam are polarized extraordinary the signal beam is polarized ordinary.

Analogously as previous derivation we obtain the following expression for the momentum conservation in cartesian formalism

$$\omega_s n_{os}(\lambda_s)x_s + \omega_i n_{ei}(\lambda_i,\theta_i)x_i = \omega_p n_{ep}(\lambda_p,\theta_p)x_p, \tag{3.35}$$

$$\omega_s n_{os}(\lambda_s) y_s + \omega_i n_{ei}(\lambda_i, \theta_i) y_i = \omega_p n_{ep}(\lambda_p, \theta_p) y_p, \tag{3.36}$$

$$\omega_s n_{os}(\lambda_s) z_s + \omega_i n_{ei}(\lambda_i, , \theta_i) z_i = \omega_p n_{ep}(\lambda_p, \theta_p) z_p. \tag{3.37}$$

Following the same derivations like in case of type-I phase-matching, i.e. by normalizing all the vectors to 1 and eliminating all variables related to signal vector, we obtain

$$\begin{aligned} &\left(n_{ep}(\lambda_p, \theta_p)\omega_p y_p - \frac{n_{ei}(\lambda_i) n_{oi}(\lambda_i)\omega_i y_i}{\sqrt{n_{oi}^2(\lambda_i) + (n_{ei}^2(\lambda_i) - n_{oi}^2(\lambda_i)) z_i^2}} \right)^2 \\ &+ \left(n_{ep}(\lambda_p, \theta_p)\omega_p z_p - \frac{n_{ei}(\lambda_i) n_{oi}(\lambda_i)\omega_i z_i}{\sqrt{n_{oi}^2(\lambda_i) + (n_{ei}^2(\lambda_i) - n_{oi}^2(\lambda_i)) z_i^2}} \right)^2 \\ &+ \left(n_{ep}(\lambda_p, \theta_p)\omega_p \sqrt{1 - y_p^2 - z_p^2} - \frac{n_{ei}(\lambda_i) n_{oi}(\lambda_i)\omega_i \sqrt{1 - y_i^2 - z_i^2}}{\sqrt{n_{oi}^2(\lambda_i) + (n_{ei}^2(\lambda_i) - n_{oi}^2(\lambda_i)) z_i^2}} \right)^2 = n_{os}^2(\lambda_s)(\omega_p - \omega_i)^2 \end{aligned} \tag{3.38}$$

Equations (3.21 - 3.24) are combined with (3.34) and (3.38) to calculate angular and wavelength distributions.

3.2.4 Some Computational Examples

In this part I will show the graphs which we calculate and use for designing the source. We start always with equation (3.34) or (3.38) for phase-matching type-I or -II, respectively, and solve this equations numerically regarding to some variable of interest, like angle of emission or emitted photon wavelength. In this chapter I will not yet show results for particular problems with specific parameter, I will qualitatively show some examples.

We implement all the methods discussed in the last part to *Mathematica* program.

In the following we look at the two cases of phase-matching, type-I and -II.

Type I

First, we investigate the momentum distribution of down-conversion photons in case of type-I phase-matching. Fixing the pump wavelength λ_p, the angle Θ_p and the wavelength of idler photon λ_i, two real solutions of equation (3.34) with respect to the variable θ_i can be found for certain values of angle ϕ_i. By varying ϕ_i for all possible solutions, a circle in momentum space can be determined as illustrated in figure 3.7. There it is also shown that a size of these circles increases with growing value of Θ_p. Thus, by tilting the crystal with respect to the pump beam we can control the opening angle, at which down-conversion photons with certain wavelength are emitted from the crystal.

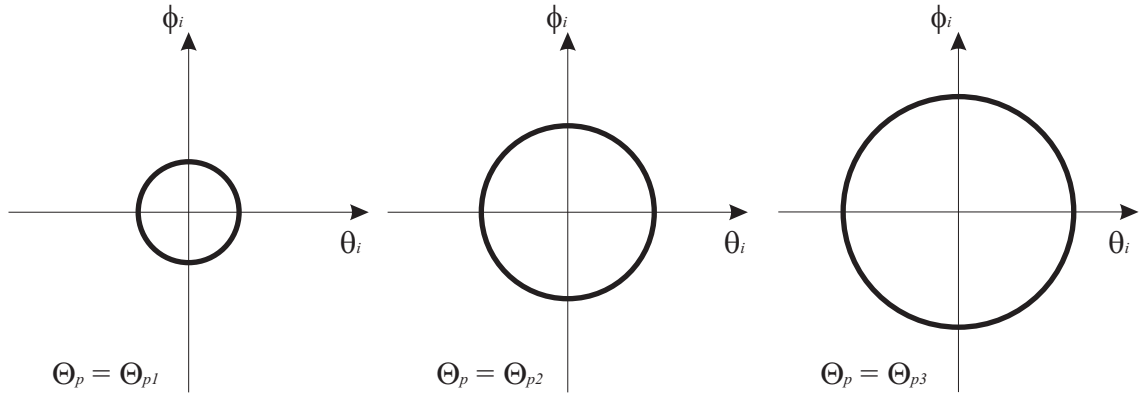

Figure 3.7: *Momentum distribution in SPDC type-I: different size of cones for different* Θ_p *where* $\Theta_{p1} < \Theta_{p2} < \Theta_{p3}$

Using equation (3.30) - (3.32) and definitions in chapter 3.2.2 we can also calculate the signal cones, but it will show up that the cones of idler and signal are exactly matched i.e. $\theta_i = \theta_s$ for arbitrary $\phi_{s,i}$. The reason is that signal and idler photons are formally indistinguishable as they have the same polarization. In (figure 3.7) the degenerate case is plotted, i.e. idler and signal have the same wavelength, which equals twice the pump beam wavelength. Looking at the non-degenerate case, i.e. the wavelength of idler and signal differs we would observe two cones with different sizes.

Next, the behavior of SPDC type-I versus the wavelength of the idler or signal photons are analyzed. To this end, numerical solutions for $\theta_i(\lambda_p, \Theta_p, \lambda_i)$ of equation (3.34) are searched. The result is displayed as function of idler wavelength λ_i. Where ϕ_i is set to 0, i.e. solutions are searched always in plane containing the pump direction and optic axis. This method is sufficient due to rotational symmetry of the cones. The results for these different angles Θ_p are displayed in figure 3.8. We again observe that for a certain wavelength λ_i, the size of cone determined by the value θ_i changes as the value Θ_p increases. Furthermore, we see that solutions are found only for certain range of idler wavelength, i.e. for parameters in plot 3.8 no solutions are found for $\lambda_i = 2\lambda_p$ for $\Theta_p = \Theta_{p1}$ and $\Theta_p = \Theta_{p2}$.

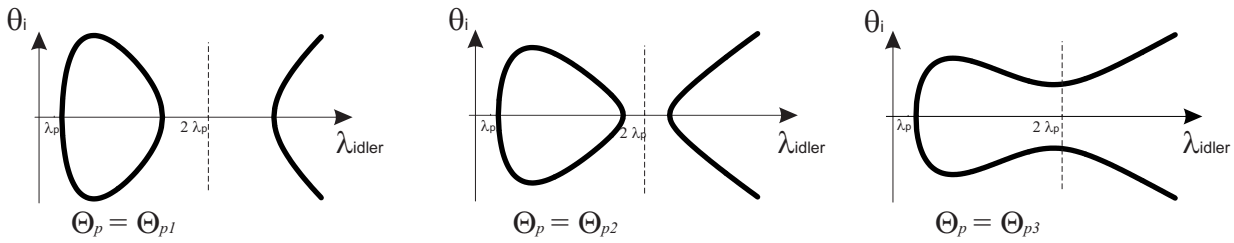

Figure 3.8: *Angular distribution in SPDC type-I versus wavelength of idler: different behavior of* θ_i *for different* Θ_p *where* $\Theta_{p1} < \Theta_{p2} < \Theta_{p3}$

In figure 3.8 one can see that for certain Θ_p there exist solutions, for which $\theta_i = 0$. Since parameter $\phi_i = 0$ here, these solutions correspond to collinear down-conversion,

where $\overrightarrow{k}_i$ and $\overrightarrow{k}_s$ have the same direction like $\overrightarrow{k}_p$. For some applications it might be also of interest to investigate the dependence of emitted wavelength on angle Θ_p assuming collinear geometry. Putting $\phi_i, \theta_i = 0$ in equation (3.34) and finding its numerical solutions for $\Theta_p(\lambda_p, \lambda_i)$ we obtain that dependency. It is displayed in figure 3.9.

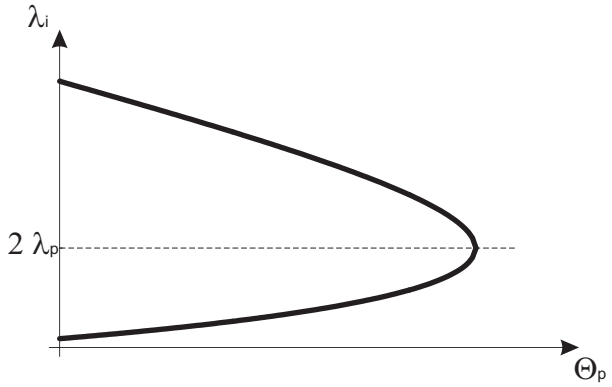

Figure 3.9: *Collinear SPDC type-I: idler and signal show the same behavior*

We observe that the phase-matching conditions cannot be fulfilled for a pump angle Θ_p above a certain value.

Type II

In this part I will describe the emission of SPDC type-II. Therefore we solve analogous to the previous section equation (3.38) with the help of the definitions in chapter 3.2.2.

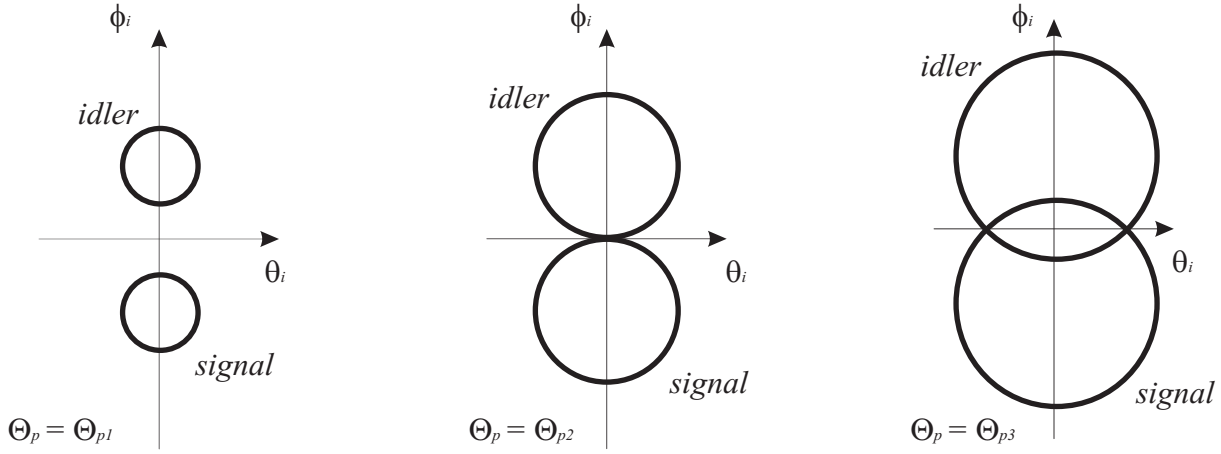

Figure 3.10: *SPDC type-II degenerate case: for different angles of pump Θ_p the cones of idler and signal changes sizes, $\Theta_{p1} < \Theta_{p2} < \Theta_{p3}$*

We will investigate again first the angular distribution of idler and signal photons. We proceed in the same way like we did for figure 3.7 with the corresponding equation and obtain 3.10.

We calculate here also cones for idler and signal similar to SPDC type-I but due to the fact that idler and signal have orthogonal polarization and they propagate in a birefringent crystal the two cones separate. Therefore we see two cones. In figure 3.10 we can see three different pump angles, parameters like Θ_{p2} and Θ_{p3} are used in many experiments to generate entangled photon pairs. At the angle Θ_{p2} we have the so-called collinear SPDC, in this configuration idler and signal can be emitted in the same direction as the pump beam. At the angle Θ_{p3} the cones are positioned in the way that the crossing point[6] of idler and signal cones show an angle to the pump beam. This configuration is called non-collinear SPDC.

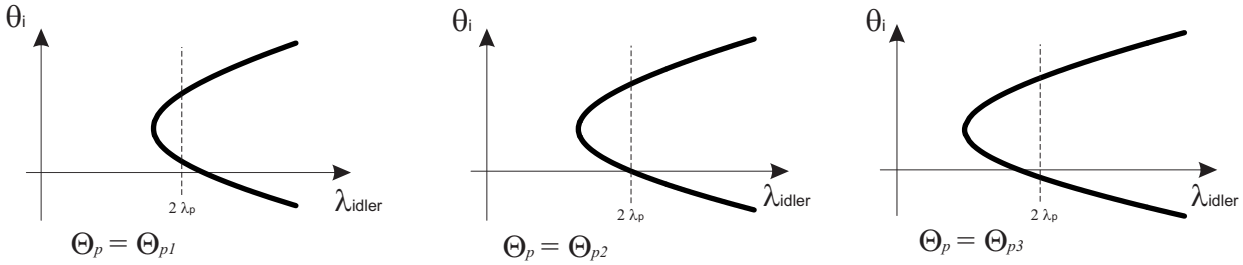

Figure 3.11: *Angle distribution in SPDC type-II versus wavelength of idler: where* $\Theta_{p1} < \Theta_{p2} < \Theta_{p3}$

For further analysis we want to investigate the emitted wavelength distribution. We solve for this purpose equation (3.38) with a given wavelength of idler λ_{idler} and will find θ_i, with ϕ_i is set to zero. We observe the in figure 3.11 shown plots for different pump angles Θ_p. These dependencies are used later for collecting a defined bandwidth of emitted photons.

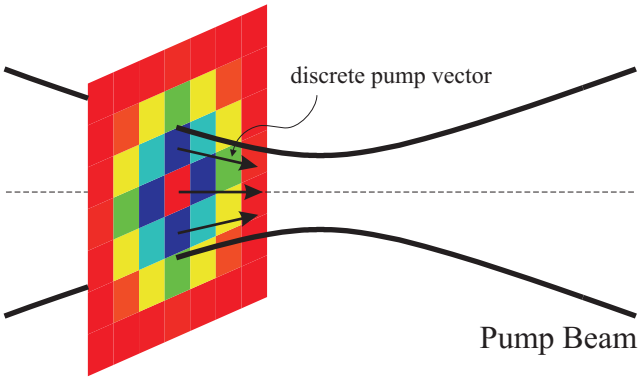

Figure 3.12: *Gaussian Pump: divided in discrete pump directions to calculate with*

One of the motivations why we defined so many degrees of freedom in the pump direction, is to allow for more than one pump direction of pump. This is necessary if we want to display the property of a gaussian beam. We take a cross section of the gaussian pump beam and divide it in as much discrete parts as we can calculate with due to gaussian optics (figure 3.12).

[6] where the entanglement can be observed

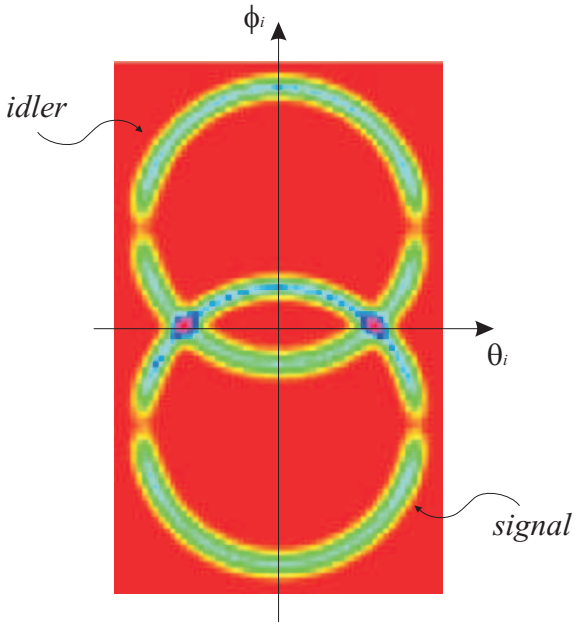

Figure 3.13: *Superposition SPDC*

These pump directions are used to calculate separately down-conversion cones, which will be superposed on a virtual screen. There we superpose the emitted photons in a certain wavelength range and obtain figure 3.13, which is still angular distribution inside the crystal. Using in 3.2.2 defined notations we calculate the angular distribution outside crystal.

3.3 Mode matching for efficient Coupling

One of the requirements of the source is to collect down-converted photons in a defined wavelength range. It showed up that the method introduced in [21] satisfy this request and guaranty also an efficient coupling for SPDC type-II. For deeper understanding it is recommended to read also [16].

The down-converted photons of the wavelength $\lambda \pm \Delta\lambda/2$ are emitted in a defined angular range $\theta \pm \Delta\theta/2$ as illustrated in figure 3.11. If we consider linear behavior of $\theta_i(\lambda_i)$ in the small region of interest we can write the following dependence

$$\Delta\theta = \frac{d\theta}{d\lambda}\Delta\lambda \tag{3.39}$$

where $\frac{d\theta}{d\lambda}$ can be read out of figure 3.11. Depending on the wavelength range $\Delta\lambda$ we want to collect we can calculate a corresponding angular range. By using a single mode fibre which collects just the TM_{00} mode[7], we can collect this angular range.

As we know already from gaussian optics in the far field of a gaussian mode we see the divergence angle θ_{div} (equation (3.8)). By using gaussian transformations we can

[7] the proof for it one can find in [22]

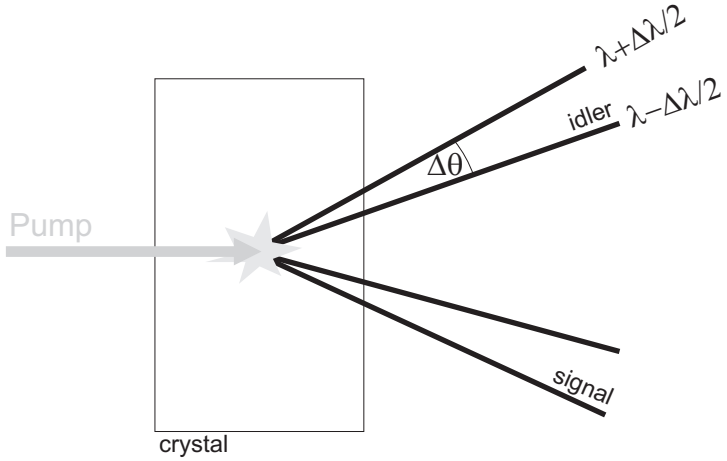

Figure 3.14: *Wavelength range of down-converted photons correspond to a defined angle* $\Delta\theta$

match θ_{div} of a single mode fibre to $\Delta\theta$. With this matching the photons which are in the wavelength range of interest lie in the mode of the fibre and can be collected by the fibre.

In [21] it is also proposed to match the waist size of the pump beam with the collecting mode of the fibre $w_{pump} = w_{collectingmode}$.

3.4 Crystal Dimensions

After designing the collecting mode in the non-collinear SPDC we will observe that not all created photon pairs can be collected by the two collecting modes, due to geometrical arrangement (figure 3.15).

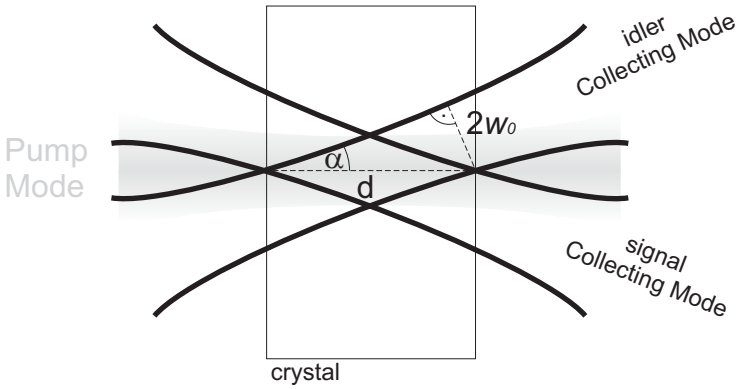

Figure 3.15: *Overlap region of the two collecting modes: in order to collect both created photons we design the overlap region in an optimized way*

Therefore only a corresponding crystal thickness makes sense. If we would use a too thick crystal we would lower our coupling efficiency due to walk-off effect in the crystal.

The overlap of the two collecting modes of idler and signal at the crystal defines the region, from which cerated photons can be collected. The length of this region gives the maximum thickness of the crystal. As we see in figure 3.15 we can approximately use the following equation for the thickness of the crystal

$$d = \frac{2w_0}{\sin \alpha}, \tag{3.40}$$

where 2α is the angle between the two crossing points of idler and signal and w_0 is the waist size of the collecting modes[8].

[8] idler and signal collecting modes have ideally the same waist size

Chapter 4

Setups for Compact Source

As we have already seen in chapter 2 sources of entangled photon pairs are very important for many applications like quantum cryptography [4], teleportation [12] etc. In former times different methods like using two type-I down-conversion crystals [5], resonant enhancement techniques [6] or using periodically poled crystals [7] have been developed to improve sources in the sense of their efficiency, robustness and size. Rather than looking for new techniques we aim at optimizing sources where photon pairs are produced via type-II down-conversion in a single non-linear crystal pumped by a laser beam and then collected into single-mode fibres.

In this chapter I will show all three setups which were designed in the scope of this thesis in detail and analyze the source performance in dependence on various parameters of pump beam, non-linear crystal and coupling optics.

I will begin with the description of a setup which is very similar to the one shown in [23]. Here a source is build using the method for increasing the collection efficiency of down-converted photons presented in [21]. The methods how to align the source are described in detail.

To further simplify the source and make it more compact we modify the setup. By replacement of the collecting optic from usual aspheric lenses to so called GRIN-lenses, it was possible to shrink the distance of crystal to the coupling optics by about 60%. Experimental problems which occurred are presented.

To reduce also the distance between pump laser and crystal we moved with it out of the focus of pump beam. Here the technique introduced in 3.3 cannot be applied. To determine the parameters of the coupling optics, ray-tracing of down-conversion photons was used. Also for this setup unexpected problems occurred, which we point out at the end of this chapter.

4.1 First Setup

4.1.1 Design of Setup

We start with giving an overview of the setup which is sketched in figure 4.1.

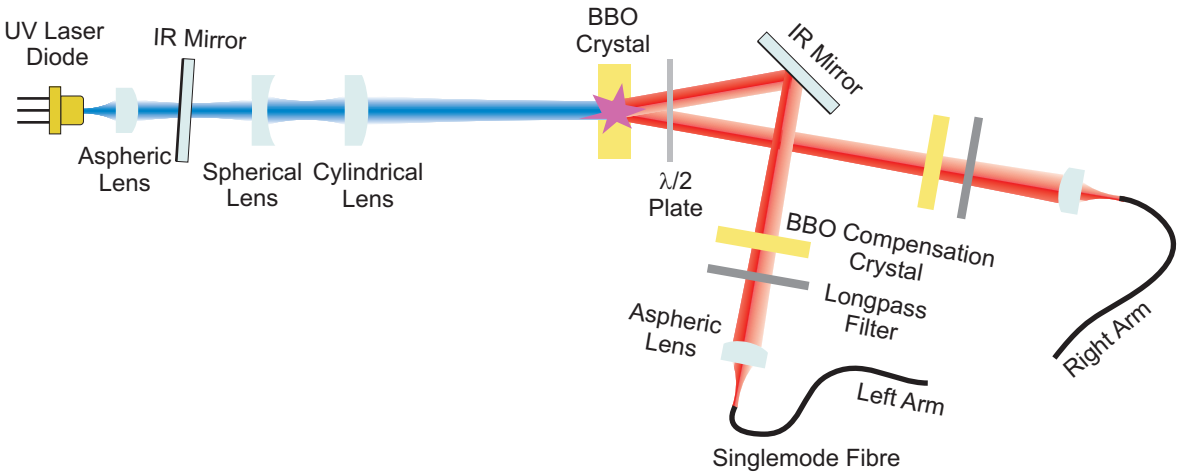

Figure 4.1: *Setup overview of the first experiment*

The single-mode laser diode emits a gaussian beam in ultraviolet (UV) spectral range at 403.5 nm. This beam is transformed with three lenses to have optimal parameters for the down-conversion process. The first, aspherical lens, and the second, spherical lens, form a telescope which focuses the pump beam to the required waist size at the BBO crystal. To compensate for the asymmetric properties of the pump beam we use a third lens. This lens is a cylindrical lens and affects only one plane of the pump beam. The laser diode emits also a small amount of light at double its wavelength, i.e in near infrared spectral region. To filter out this unwanted emission an infrared mirror with a very good transmittance for UV light is placed behind the laser diode.

The laser diode is oriented in such a way that the pump beam polarization is vertical. A non-linear crystal is placed in waist position of the pump and oriented such that extraordinary polarization corresponds to vertical direction. With such configuration, the downconversion type-II can be observed. Under proper tilt of the crystal with regard to pump beam, the downconversion cones intersect each other as described already in chapter 3.2. The photons emitted along the intersection directions are aimed to be collected, as they form an entangled photon pair.

In our experiments we use a negative uniaxial crystal, namely a Beta-Barium Borate ($\beta - BaB_2O_4$) crystal, often called BBO. Due to the walk-off effects in a BBO crystal, we have to place additional optical components, in order to provide mutual indistinguishability of down-conversion photons and thus obtain entanglement. As will be explained later a $\lambda/2$ plate together with BBO crystal of the half thickness can compensate walk-off effects. To filter out the residual UV light coming from laser diode, long-pass filters are used.

Finally, aspherical lenses are used to collect the entangled photon pairs into single-mode fibres. We mirror one of the arms to reduce the size of the source.

Angular distribution SPDC and mode matching technique

In this part the angular distribution of SPDC type-II is calculated for our particular setup using the methods introduced in chapter 3. For this purpose we use the following Sellmeier equations for the refractive indices in a BBO crystal [24]

$$n_o^2(\lambda) = 2.7359 + \frac{0.01878}{\lambda^2 - 0.001822} - 0.01354\lambda^2 \tag{4.1}$$

$$n_e^2(\lambda) = 2.3753 + \frac{0.01224}{\lambda^2 - 0.001667} - 0.01516\lambda^2 \tag{4.2}$$

where λ is given in units of μm.

In order to achieve efficient coupling the idler and signal cone must intersect perpendicularly as required for the mode matching technique introduced in 3.3. Assuming this configuration we find the corresponding angle Θ_p between OA of the crystal and the pump direction, by applying theoretical tools showed in 3.2. For our particular pump beam wavelength of $403.5nm$ and for the degenerate case, we calculate $\Theta_p = 42,84°$. For this specific angle the crossing point of idler and signal (figure 4.2) has the following coordinates in momentum-space

$$\begin{aligned} \theta_{i,s} &= 3.26°, \\ \phi_{i,s} &= 0°. \end{aligned}$$

Therefore the collecting optics must be positioned at $\theta_{Cross} = 3.26°$ with respect to pump direction.

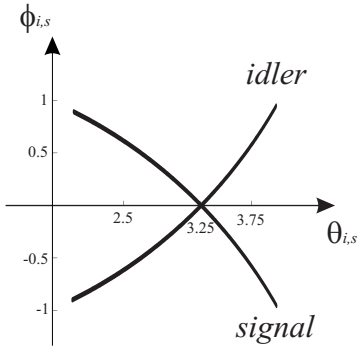

Figure 4.2: *Crossing point of idler and signal cone λ@807nm: for* $\Theta_p = 42,84°$ *we get a crossing point at* $\theta_{i,s} = 3.26°$

The collecting optics will accept a certain angular range $\Delta\theta$ around the coordinates 4.1.1. According to equation 3.39 $\Delta\theta$ corresponds to a particular spectral bandwidth $\Delta\lambda$.

In our case we choose $\Delta\lambda$ to be 6 nm. This value seems to be a reasonable compromise as a too narrow spectral bandwidth would lower the amount of the collected

entangled photon pairs. On the other hand a very broad spectral bandwidth would decrease the quality of produced entanglement.

We use the dispersion relation $\theta_i(\lambda_p, \Theta_p; \lambda_i)$ and can directly determine $\Delta\theta = 0.16°$ for our particular value for $\Delta\lambda$ (figure 4.4). But for further calculation we consider $\Delta\theta_{SPDC} = 0.19°$, due to angular uncertainty of the pump mode. Using equation (3.8) we calculate $w_{SPDC} \approx 75\mu m$. The collecting optics is designed in such a way that the mode provided by a single-mode fibre is imaged a waist size of $75\mu m$ on the crystal. It is easy to retrace that if $w_{Pump} > w_{SPDC}$, we cannot collect all photons created, therefore we also match the pump waist size to the waist size of the collecting mode.

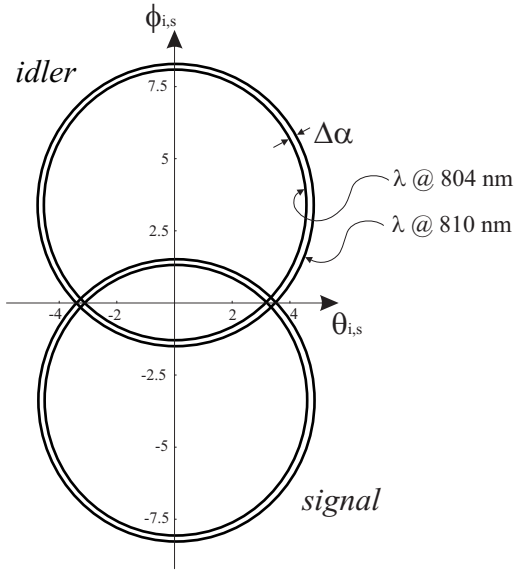

Figure 4.3: *Angular distribution for a spectral bandwidth of 6 nm: with* $\Theta_p = 42,84°$ *and* $\lambda_p = 403.5nm$

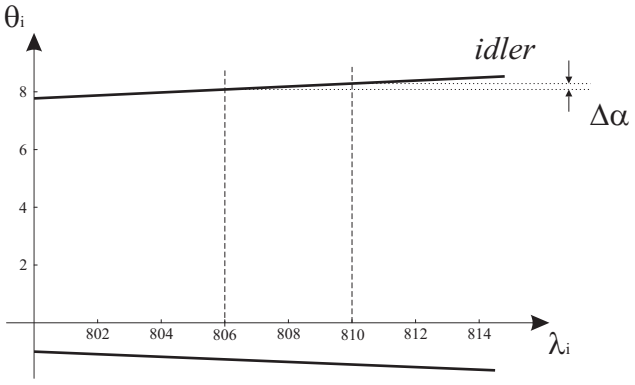

Figure 4.4: *Dispersion relation: with* $\Theta_p = 42,84°$ *and* $\lambda_p = 403.5nm$ *we get for* $\Delta\alpha = 0.16°$*, in this figure* $\phi_i = 0°$

Applying the obtained results from above discussed calculations we can fix all the

parameters of the source. In the following starting from pump beam and ending by collecting optics we describe step by step the design source in more detail.

Pump preparation

The pump beam for the SPDC is provided by a single-mode laser diode [Nichia , NDHV310ACA] with a maximum output power of 26 mW. The laser diode is driven in the constant current mode. Above a certain driving current it starts to lase and the optical power grows linearly with current. The laser diode is mounted in an aluminium case, which is temperature stabilized at 18° C using a peltier element. The spectrum of the laser diode is shown in figure 4.5(a), the fitting, gaussian distribution to the measured data[1] has a peak value at 403.4 nm. Unfortunately another spectral peak at exactly double the wavelength, i.e. at 807 nm, was observed (figure 4.5(b)). The intensity of the emitted at 807 nm was estimated to at least four order of magnitudes weaker compared to the intensity at 403.4 nm. In the experiment we are working exactly in this wavelength range and all our filters are transparent for this wavelength, therefore we need to block this second peak. This is done with a mirror with high reflection (HR) for 807 nm and high transmission (HT) for 403 nm.

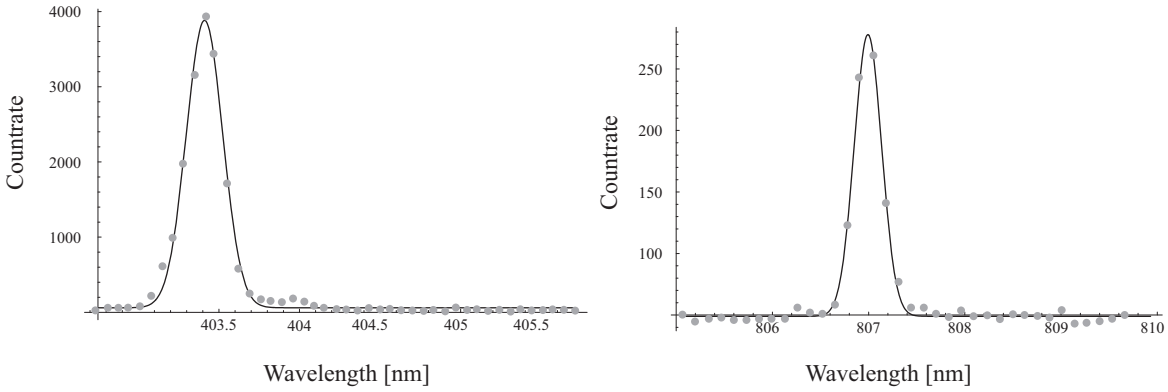

(a) *Main peak @ 403.4 nm (gaussian fit)* (b) *Side peak @ 806.99 nm (gaussian fit)*

Figure 4.5: *Emitted spectrum of laser diode: Wavelength (measured value (•) fitted to gaussian distribution (-)) vs. count rate*

In figure 4.6 we see the setup of the pump preparation. An aspherical collimation lens with a focal length of 4 mm is used in combination with a spherical lens with a focal length of −15 mm the beam is focused to a distance of 180 mm. Due to the geometrical properties of the laser diode cavity [25], the beam shows asymmetries in horizontal and vertical plane. We measure different M^2-Factors in the two planes. To compensate for this asymmetries we use a cylindrical lens with a focal length of 150 mm. With this configuration we obtain a circular shaped beam whose intensity distribution has gaussian profile. Its waist size is 75 μm as required by the calculation from the previous section.

[1] the spectrum is measured with a commercial spectrometer PC2000 from Ocean Optics

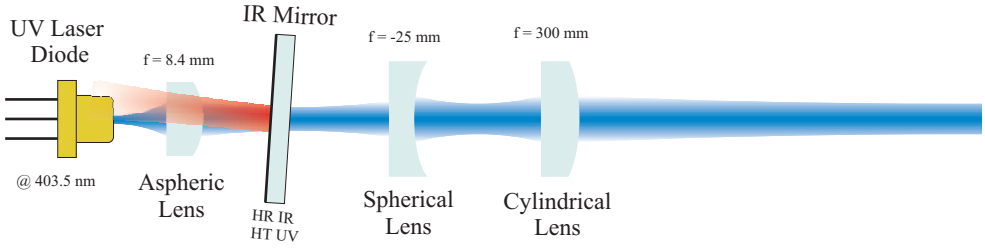

Figure 4.6: *Engineering the pump mode*

Crystal dimensions

Knowing the parameters of collecting mode w_{SPDC} and θ_{Cross}, we determine the maximum thickness of the crystal as defined in 3.4 to be 2.6 mm. For the experiment we therefore used a 2 mm thick 7x7 mm BBO[2] crystal. This crystal is cut in such a way that by placing the crystal perpendicular with respect to pump beam direction, the angle between OA of the crystal and pump is the calculated angle ($\Theta_p = 42.84°$). Both surfaces of BBO are antireflection coated at both 403 nm and 807 nm.

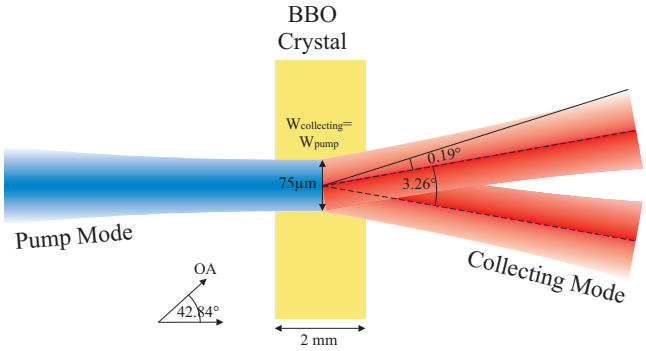

Figure 4.7: *The design of crystal*

Walk-off compensation and collection optics

Using the definitions from 2.3.3 and 2.3.3 assuming the parameters of the BBO crystal, we calculate for the transversal walk-off the value of ≈ 145 μ m and for the longitudinal walk-off ≈ 0.7 ps. By comparing the transversal walk-off with the pump waist size of 75 μm, and the longitudinal walk-off with the coherence time of the emitted down-converted photons, we see that there is a need for compensation of this two effects. It will show up that by placing a $\lambda/2$-Plate at 45° and an additional compensation BBO crystal with the half thickness of the main crystal, in the path of the collecting mode we can almost[3] compensate the transversal walk-off and compensate the longitudinal walk-off. In this way high quality of polarization entanglement can be restored.

[2]Foctek Photonics, Inc. [24]
[3]the elliptical shape of the extraordinary beam cannot be compensate to be circular

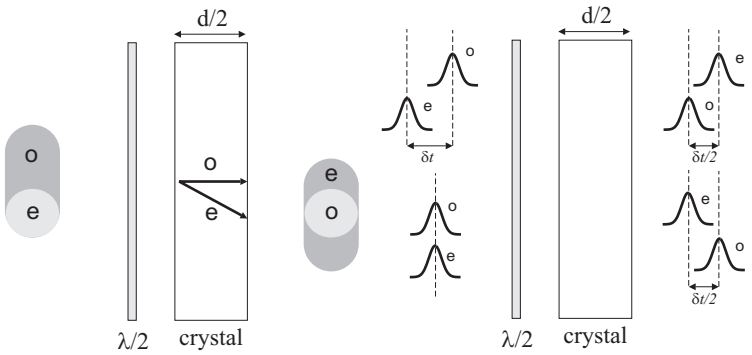

(a) *Transversal walk-off compensation* (b) *Longitudinal walk-off compensation*

Figure 4.8: *Compensation of transversal and longitudinal walk-off, with a* $\lambda/2$*-Plate at* 45° *and a 1mm thick BBO crystal*

The $\lambda/2$-Plate at 45° exchanges the polarization of the downconversion photons. An extraordinary beam is transformed to a ordinary and vice versa.

By passing a compensation BBO crystal, which is oriented in the same way as the down-conversion crystal, the extraordinary beam is diverted and the center of the ordinary and extraordinary beams will overlap again (figure 4.8(a)). At the same time also the longitudinal walk-off is compensated. The two photons might be distinguishable in arriving time, but one cannot determine from this the polarization of the photon, please see figure 4.8(b). The photons are thus indistinguishable.

Additionally by tilting the compensation crystal in one of the collecting arms, the relative phase ϕ between $|HV\rangle$ and $|VH\rangle$ in the created state

$$|\psi\rangle = \frac{1}{\sqrt{2}}(|HV\rangle + e^{i\phi}|VH\rangle) \tag{4.3}$$

is changed. This is due to the fact that the relative delay in optical path of created photons is altered by the tilt of the birefringent compensation crystal. For $\phi = 0$ and $\phi = \pi$ we can prepare directly $|\psi^+\rangle$ and $|\psi^-\rangle$, respectively. By placing an additional $\lambda/2$-Plate at 45° in one of the collecting modes one can also prepare $|\phi^+\rangle$ and $|\phi^-\rangle$ states. Thus we see we can easily prepare all the Bell states.

In figure 4.9 we see the whole compensation and collecting part of the setup. With an aspherical lens we couple the intended angular range $\Delta\theta_{SPDC}$ in a single-mode fiber with a mode field diameter of 5.2 μm. In order to keep the distance from the crystal to single-mode fiber small we use a lens with a relatively short focal length of $7.5mm$. Using such lens this distance was fixed to $\approx$ 280 mm. As a long-pass filter we use RG 715[4], which has a transmission at $400nm$ about 10^{-3}% and at 800 nm about 91%. An additional antireflection coating of this filter increases the transmission of RG 715 at 800 nm to 98.5%.

[4]SCHOTT AG.

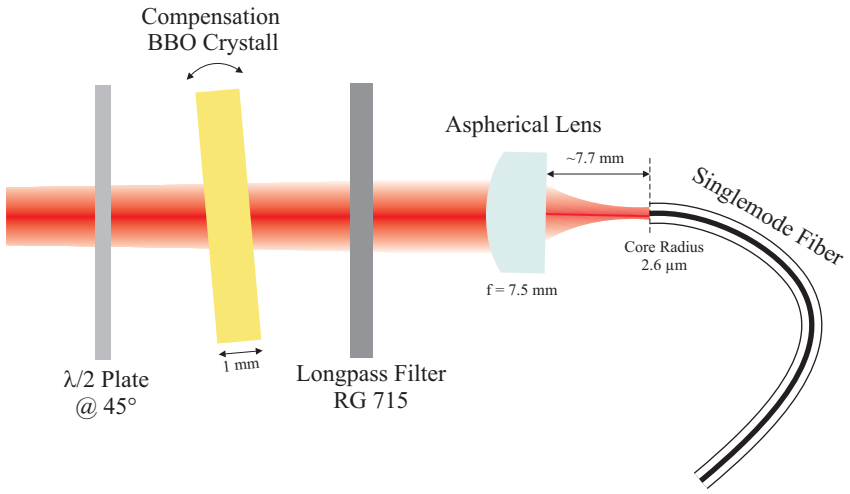

Figure 4.9: *The design of compensation and coupling*

4.1.2 Methods of Aligning

To be able to analyze the state which we are preparing, we need to detect and analyze single photons. In our experiment we use passively quenched Silicon-Avalanche-Photodiodes[5] (Si-APDs). These photodiodes are fibre coupled to multi-mode fibres and are mounted in an aluminium case. To lower the dark-counts they are cooled down to $-23°$ with a Peltier element. The dark-counts of the diodes are approximately 100 counts per second and the detection-efficiency is about 35%. After detection of each photon the detector electronics sends a NIM-pulse, which is converted to a TTL-signal which can be read out from a computer and be displayed. For us it is important to look at photons created at the same time. In the first steps each collecting arm is connected to a detector. If two photons are arriving at the detectors in the same time window, also called *coincident window*, a coincidence pulse is generated. We chose a $8ns$ broad coincident window. In this way we know that these two photons are created by SPDC. It can also happen that accidently two photons are arriving in the same time window, but for our pump power and the mentioned coincident window the number of these events is negligible.

In principle the alignment of the source means to move with the two collecting optics[6] into the crossing point of idler and signal cones at degenerate wavelength. Due to the fact that the intensity of the down-converted light is very low it is not possible for us to position the couplers directly to the crossing point. To do it indirectly there are many technics. I will present the most interesting ones.

As we know from chapter 4.1.1 that the angle between pump and the intersection point is $\theta_{Cross} = 3.26°$, we can approximately position the coupler with the help of an alignment laser at these angles. The two couplers are mounted on translation-stages[7],

[5] Perkin Elmer Type C309025
[6] we refer as *coupler* to it
[7] the translation-stages are operating in horizontal and vertical planes

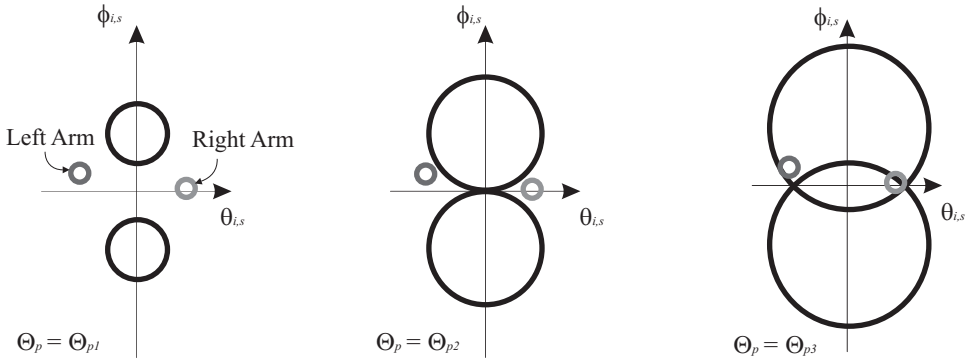

Figure 4.10: *Wrong position of the couplers:*

which makes it possible to move in $5\mu m$ steps in horizontal and vertical plane. In further alignment methods we use these translation-stages to change the position of the couplers.

In the following I want to introduce two methods which allow us to move more precisely into the crossing point. The first method uses an interference filter to select exactly the degenerate case. The second method uses the spectrum which is collected to predict how far we are away from the cross section.

Looking at figure 4.10 we see how the cones (for degenerate case) change their sizes with respect to Θ_p. By placing an interference filter in front of the coupler just photons with the degenerate wavelength are passing. Interference filters have the property just to be transparent for a narrow bandwidth at a designed wavelength. We are using interference filter designed for $807nm$ and a bandwidth of $5nm$.

Plotting the single photon count rates of each coupler arm versus Θ_p, we can estimate which kind of misalignment exists. Figure 4.11(a) shows the plot before aligning. We can observe that the left arm sees two intensity peaks, this is an indicator for misalignment in vertical direction and we observe also a gap between left and right arm, which points on a misalignment in horizontal plane. By moving with the left coupler in vertical direction we can achieve that we just see one intensity peak (figure 4.11(b)) and by moving with both couplers towards each other we align also for horizontal plane (figure 4.11(c)). Due to the fact that we moved very close to the crossing points the coincident count rates increase. By putting polarization filters at H or V in front of the couplers, we can even work more precisely because we just see either idler or signal cones.

Another way to ensure the right position of the couplers is to analyze the spectrum of the collected mode. As already discussed the single-mode fiber collects a certain spectral bandwidth, the peak value of this spectrum is depending on the exact position of the coupler. This fact we are using to estimate where, in respect to the degenerate case, the coupler is standing. We measure the spectrum of collected idler and signal separately by putting a polarization filter at H and V respectively in front of the coupler of interest.

The spectrum is recorded with a home made single photon spectrometer, no com-

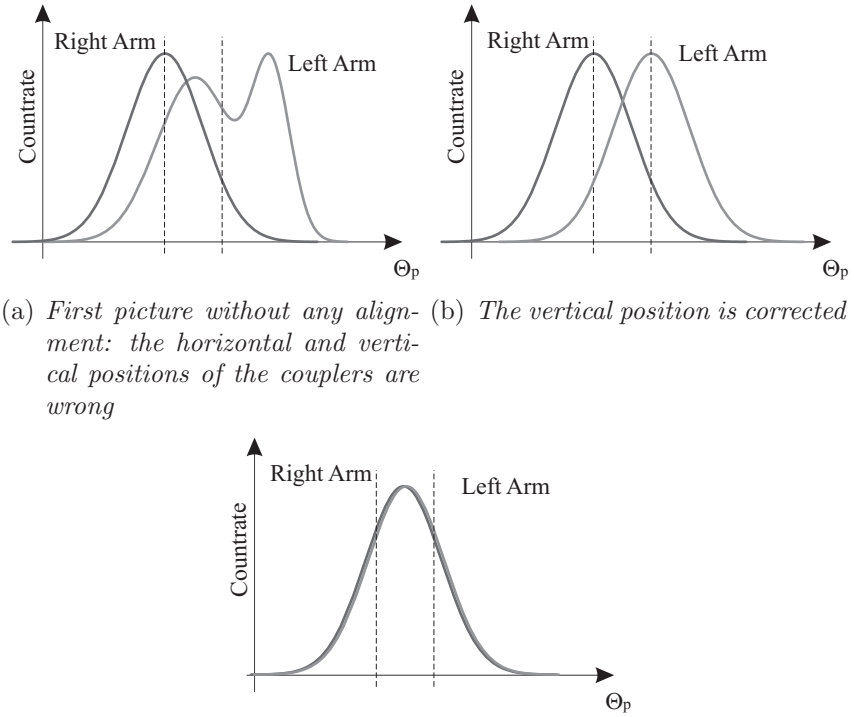

(a) *First picture without any alignment: the horizontal and vertical positions of the couplers are wrong*

(b) *The vertical position is corrected*

(c) *The horizontal positions are corrected*

Figure 4.11: *With the help of interference filter we can look at degenerate photons: three steps of aligning are shown*

mercial one can meet our demand to detect also single photons.

In figure 4.12 we see a graph, which was generated with real setup parameters[8], where the spectral distribution of idler and signal is shown. Measuring the spectrum of idler and signal we can refer back to the position of the coupler. In figure 4.13(a) - 4.13(c) we see three recorded points and see in figure 4.12 the corresponding positions. It is not obvious how far we need to move to go from one starting point to the final crossing point of the degenerate wavelength. With an additional reference point we can hit the aimed point very precisely.

Unfortunately it turned out, that to be positioned at the crossing points of the degenerate cones, is not a guarantee to have a pure entangled state. To ensure this we scan carefully in all directions.

4.1.3 Results

In the optimal position of the coupler, where we expect the highest quality for entanglement, we obtain the count rates for single count in both arms and the coincidence rates which are shown in figure 4.14. From this numbers we can calculate around 800

[8]the following example was performed on a source where the pump wavelength was $402.5nm$, therefore the degenerate wavelength is at $805nm$

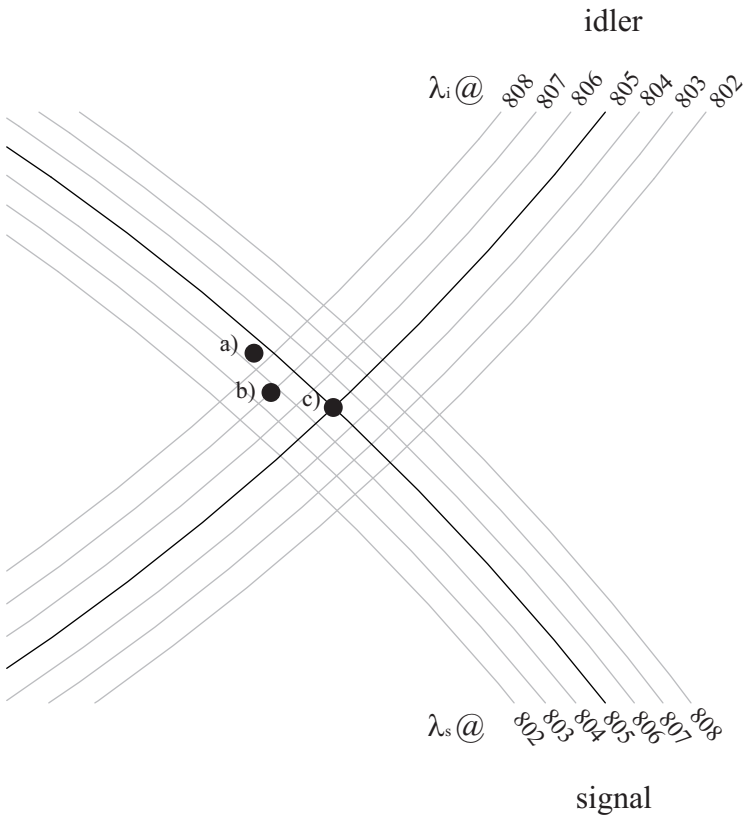

Figure 4.12: *Spectral distribution of idler and signal in the right intersection: Looking separately at the spectrum of idler or signal one can attach the right position of the coupler in respect to the degenerate case*

coincidences per 1 mW. The coincident to single ratio was 34%, this is a measure for the probability to detect a photon and its relatively low value arises due to two main effects. Firstly due to the efficiency of the detector APD's and secondly due to the not efficient coupling to the single-mode fibres.

A very common way to find out whether the measured coincidences gives an entangled state is to look at the *correlation function* in different basis. We analyze the polarizations of the photon pairs by placing polarization filters in their path. Keeping one of the polarization filters at H and varying the other one we expect to see an sin^2 curve, where we expect at a parallel arrangement of the polarization filter the minimum value for the count rates and a maximum for an orthogonal arrangement. Because we can rewrite the $|\psi^-\rangle$ state, which we intent to produce, in the +/- base

$$\begin{aligned} |\psi^-\rangle &= \frac{1}{\sqrt{2}}(|HV\rangle + |VH\rangle) \\ &= \frac{1}{\sqrt{2}}(|+-\rangle + |-+\rangle) \end{aligned} \tag{4.4}$$

we expect by measuring the correlation function in the +/- base to observe the same behavior as in H/V basis (figure 4.15).

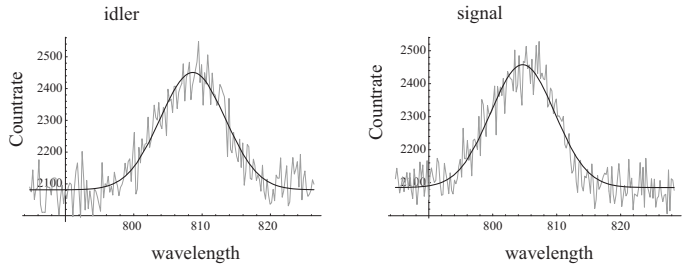

(a) *Spectrum of idler and signal: idler: intensity peak @ 808.6 nm; signal: intensity peak @ 804.6 nm*

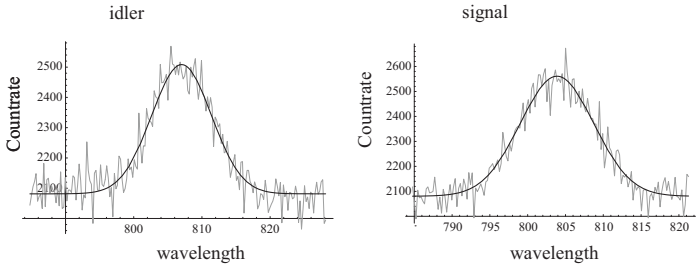

(b) *Corrected for horizontal and vertical misalignment, but not yet finished: idler: intensity peak @ 807 nm; signal: intensity peak @ 803.8 nm*

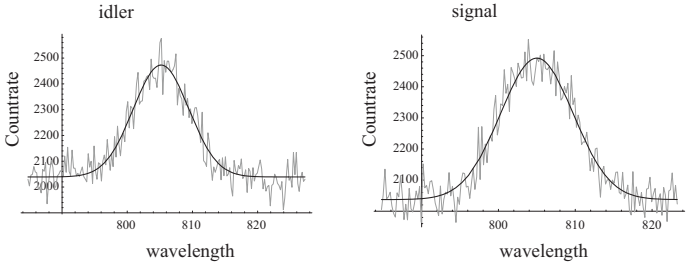

(c) *Spectrum in the crossing point: idler: intensity peak @ 805.2 nm; signal: intensity peak @ 804.99 nm*

Figure 4.13: *By putting polarization filters in front of the coupler one can measure separately the spectrum of idler or signal, measured value (−) gaussian fit (-)*

A measure for the contrast of the curves shown in figure 4.15 is the *visibility* and is defined like the following

$$v = \frac{R_{max} - R_{min}}{R_{max} + R_{min}} \tag{4.5}$$

where $R_{max,min}$ are the count rates in the maxima and minima. For the fitted cures in figure 4.15 we get in H/V basis a visibility of 99.55% and in +/- basis 94.20%.

Also count rates where measured to violate the CHSH inequality, which were introduced in 2.1.2. With an integration time of 1 sec for each set of angle we obtain

$$S = 2.75251 \pm 0.0132494 \tag{4.6}$$

where S is defined like equation 2.2. This corresponds to a violation by 57 standard

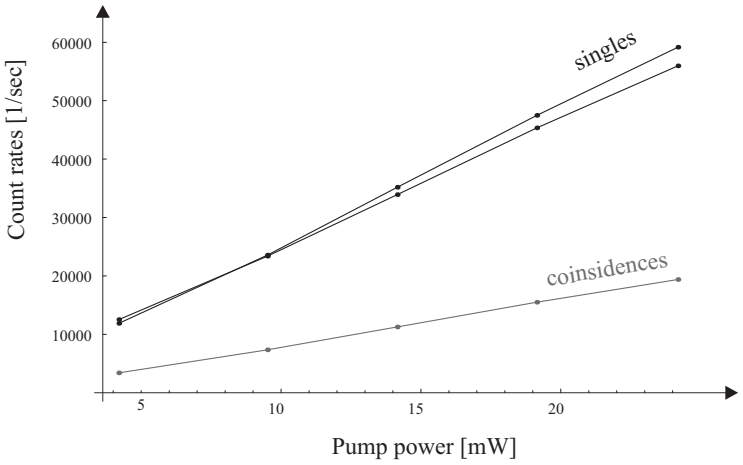

Figure 4.14: *Single count rates (•) and coincident count rates (•) versus pump power*

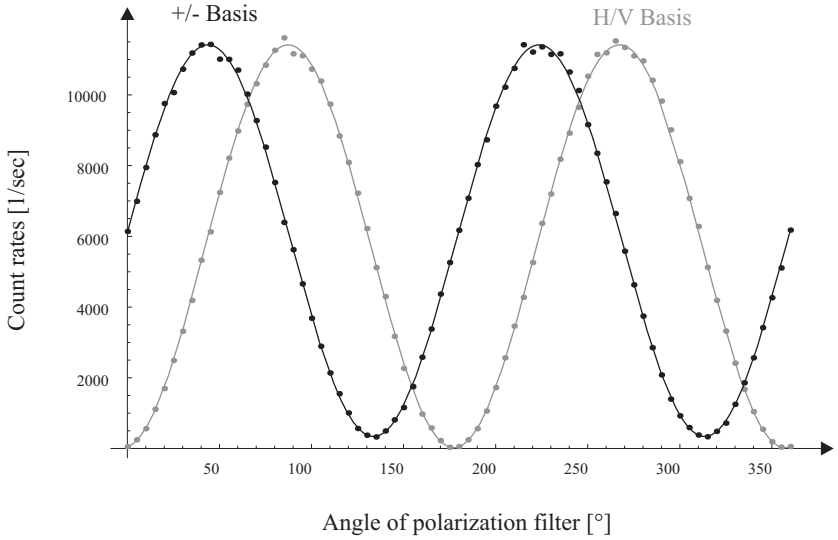

Figure 4.15: *Polarization correlation function: H/V Basis (•) and +/- Base (•)*

deviations of the classical bound.

4.2 Advantages by the use of GRIN-Lens

4.2.1 Motivation and Setup

The source presented in the last part showed up to be a reliable source of polarization entangled photon pairs with relatively good performance. However, the size of the source is not satisfying. With conventional lenses it was not possible to reduce significantly the distance from crystal to collecting optics more than it was done in chapter 4.1. Otherwise we would have to accept lower coupling efficiencies. Gradient Index Lens (GRIN Lens), however, promised to keep our requirement to match the angular

distribution of down-converted light $\Delta\theta$ to angular width of the spatial mode collected into single-mode fiber, while reducing the distance between crystal and lens.

GRIN lenses are cylindrical shaped lenses with a continuous radial change of refractive index from the optical axis to the edge of the lens (figure 4.16). Similarly to a conventional lens, the optical path length of light changes with distance to the optical axis of the lens. By varying the thickness of the GRIN lens it is possible to change its focal length [26].

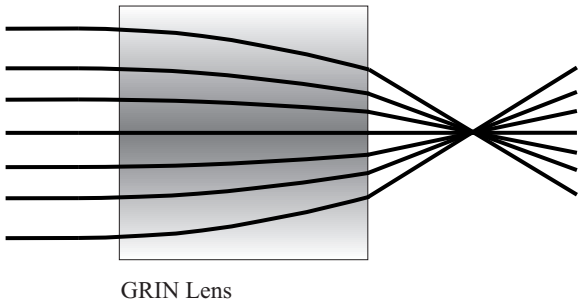

Figure 4.16: *GRIN Lens: the retractive index changes gradually along the radial distance along the center*

In our experiment we use custom made GRIN lenses[9], which are directly glued to a single-mode fiber. The thickness of the lens and the gradient of the radial change of refraction index was chosen such that it provided TM_{00}[10] focused at 100 mm behind the lens. According to data sheet given by manufacturer the waist size should be 75 μm. Note that this value corresponds to the calculated waist size w_{SPDC} (see section 4.1.1).

To characterize the GRIN lenses we launched a laser light at 780 nm into the single-mode fiber and recorded the out coming mode with a CCD camera at various positions behind lens. Three obtained cuts of this mode are shown in figure 4.17. Although the

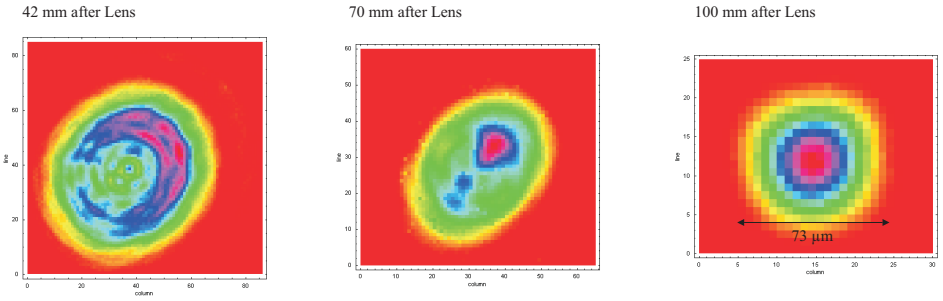

Figure 4.17: *Gaussian mode profile provided by the GRIN Lens: focal point at 100 mm, waist size 73 μm*

intensity distributions before the waist position have not a gaussian shape, the profile in waist is satisfying. We measured a waist radius of 73 μm.

[9]GRINTECH GmbH
[10]wavelength around 800nm

To characterize the coupling efficiency, another measurement was performed. For this purpose we prepared, by using laser light coupled into a single-mode fiber[11] and a aspheric lens (f=11 mm), a gaussian mode with the waist size of 73 μm matched to the mode provided by the GRIN lens. By optimizing the coupling efficiency of this mode into the single-mode fibre of the GRIN lens, we achieved the maximum at 100 mm behind waist position as expected. In such a way, no more than 70% of laser light was coupled. Note that for conventional coupling methods using aspheric lenses efficiencies of about 90% can be achieved. From these results we can expect lower efficiency of the source measured by the count rates. On the other hand the distance between crystal and collecting optics can be reduced by 65%, from 280 mm to 100 mm.

The implementation is shown in figure 4.18. In contrast to the source presented

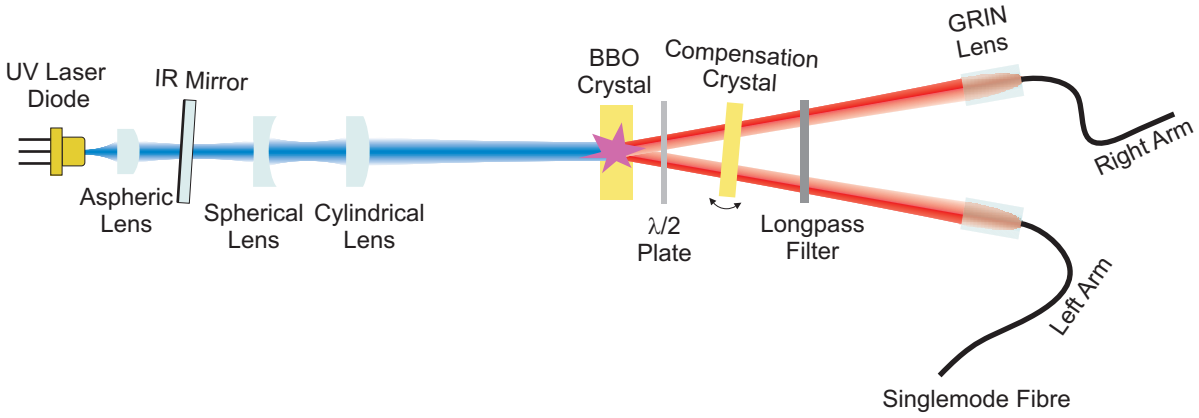

Figure 4.18: *GRIN Source*

in chapter 4.1 there is no need to mirror one of the collecting arms. The small size of the GRIN lenses allows us to position them very close to each other. The lenses are mounted on translation-stages to be positioned in horizontal and vertical plane. Otherwise all the components and design parameters of the source presented in 4.1 are used. Unlike the previous setup we put only one compensation crystal and one long-pass filter inside both collecting modes. As already discussed the compensation crystal is, beside compensating the longitudinal and transversal walk-off, also used to switch between two of the Bell states, therefore we need to position it in the way that we can introduce an optical path length difference between the photons forming an entangled pair. To align the source methods introduced in 4.1.2 can be applied.

4.2.2 Result and depolarizing effect

First, the single-mode fibers from the source were directly connected to the APDs and count rates were recorded. The slope of 200 coincidences per second and mW of pump power was observed. The efficiency of this source is thus lower compared to the previous setup, as expected from the characterization of GRIN lenses.

[11] THORLABS P1-3224

Unfortunately, we could not achieve a higher visibility than 94% in H/V basis and 90% in +/- basis. This was due to the fact that fibre coupled GRIN lenses introduced a depolarizing effect which was not possible to compensate by using standard methods like using polarization controller or a combination of wave-plates. To investigate this effect more in detail we performed a quantum process tomography, it allows to characterize a quantum mechanical process $\mathcal{E} : \rho_{in} \rightarrow \mathcal{E}(\rho_{in})$ of any kind. The basic idea is to use a so-called tomographic set of input states P_{in} [12] and estimate the corresponding output state P_{out} (which will be our basic set of output states) via quantum state tomography (QST) [27]. QST is a technique to fully characterize a quantum state via a certain (also tomographic) set of measurements. As any input ρ_{in} can be decomposed into the tomographic set P_{in} with certain weighings and as the process is assumed to be linear we can reconstruct the corresponding output by a linear combination of the basic set of outputs states P_{out} with the same weighings. Thus the action of the transformation $\mathcal{E}$ is known for any possible input ρ_{in}. To learn something from this information it is necessary to find a convenient description. For this the process is decomposed into a basic set of unitary transformations (which is always possible). In our case the decomposition is just for one qubit and therefore we can take the Pauli matrices $\sigma_0 = 1, \sigma_1 = \sigma_z, \sigma_2 = \sigma_x, \sigma_3 = \sigma_y$.

$$\mathcal{E}(\rho_{in}) = \sum_{i=0,j=0}^{3} \chi_{ij} \sigma_i \rho_{in} \sigma_j \tag{4.7}$$

The coefficients χ_{ij} completely describe the process and are depicted in 4.19. We expect the process to be just the unity, i.e. there should be no action on the state of the photon, this would be represented by a single entry at the left corner. The measured matrix, however, has only a contribution of about 90% there and also entries in all other elements. This points out on a depolarization effect, but also other unknown effect, which needs to be investigate more in detail.

Due to specifications about GRIN lenses from manufacturer we know that the lens itself has a polarization preservation of at leat 99%. We suppose that the depolarization effect is caused at the connecting point between the lens to the fiber. We conclude that the performance of the presented source is significantly lower compared to the one which utilizes aspherical lenses.

4.3 Moving with Crystal out of Pump Waist

4.3.1 Motivation and Setup

Our last setup was partly inspired by ideas of D. N. Klyshko [28] and the experimental work of C. H. Monken et al. [29]. Therein the configuration is presented where the pump beam is focused to a plane behind the crystal where the detectors are positioned. In their experiment the downconversion photons were directly collected by detectors

[12] any physical state can be described by a linear combination of such a tomographic set

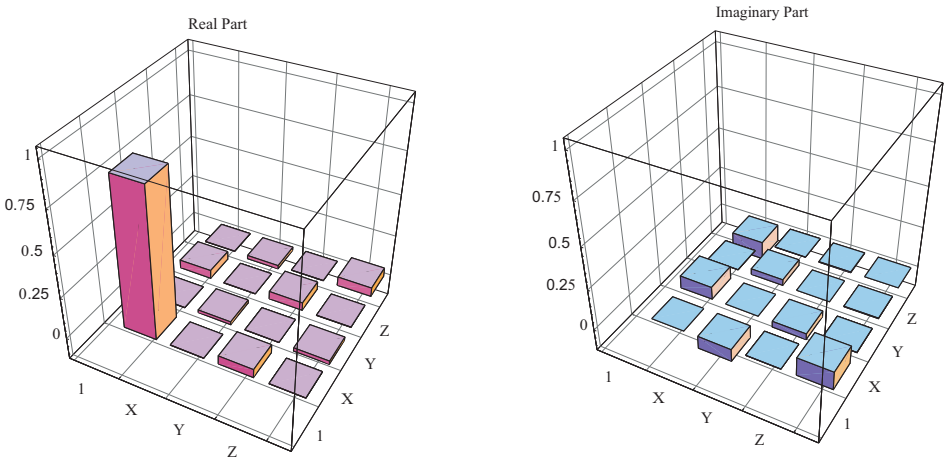

Figure 4.19: *Density matrices*

without using single-mode fibres and a relatively high single to coincident ratio was observed. With such arrangement, but by using single-mode fibers, we hoped to reduce significantly the size of the source, while still achieving high efficiency of the setup.

In former experiments we always placed the crystal into the waist position of the pump mode. With a good approximation, we could restrict the down-conversion process to a infinitely small transversal area and pump beam was described by a single $\boldsymbol{k}$-vector. For the arrangement where the crystal is out of focal position of the pump beam such simplifications cannot be assumed and more complicated calculations has to be accepted. For calculations a range of pump $\boldsymbol{k}$-vectors must be considered.

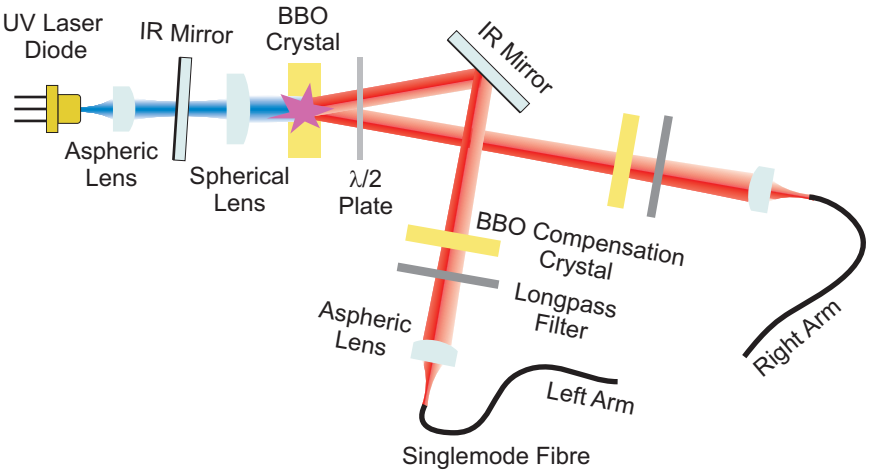

Figure 4.20: *Source setup: the crystal is not in waist of the pump mode*

In figure 4.20 we see the experimental setup where the crystal is moved closer to the laser diode out of the pump beam focus. This configuration enabled us to significantly reduce the size of the whole setup. In the following we describe the way how to determine the specific parameters of pump beam and collection optics. For this purpose simulations introduced in chapter 3.2.4 are used.

As already mentioned before the description of the pump beam has to be changed. The cross section of the pump beam at crystal surface is much bigger than in its waist and the curvature of the beam at this position defines for every point in this cross section another angle to the center of the beam. Therefore we divide the pump cross section into small squares. In view of gaussian optics every of this squares has an individual intensity and $\boldsymbol{k}$-vector. For every of this squares we solve the phase-matching conditions and obtain with the use of equation (3.38) the emission directions of idler and signal photons. Assuming the spectral bandwidth of 5 nm around the degenerate wavelength for the down-conversion photons we could for every square calculate the intensity distribution of SPDC photons at any distance behind crystal. For explanation, see also section 3.2.4. All resulting intensity distributions for every square are superposed with a weighting according their relative intensities. Here we also take the distribution of this squares in space into account. This method allows us to simulate the whole process. We can assume any parameters of the pump beam and any crystal position.

We used this method to simulate the down-conversion intensity distribution assuming different pump beam asymmetries. Since for the design of the source only the transverse profile of the intersection between idler and signal is of importance we do not calculate the whole cones. In figure 4.21 the obtained results are displayed. We see an interesting behavior. The intersection of idler and signal is not completely circular by pumping the crystal with a circular gaussian beam (figure 4.21(a)). The intersection shows even more ellipticity, if we pump it with a beam with smaller waist size in vertical plane[13] (figure 4.21(b)). This is due to the fact that the vertical[14] distributed angles in pump beam gives different angles to OA of the crystal, as we know this causes cones with different sizes. But the angles distributed in horizontal plane in the crystal does not change the angle to OA. Therefore, by pumping the crystal with a beam having the smaller waist size in horizontal plane, we observe the opposite effect, the intersection becomes more circular. Since the provided mode by the single-mode fiber has a circular shape, the setting studied in figure 4.21(c) is also used for our setup.

In former experiments we always compensated the asymmetries of the pump beam provided by the laser diode with the help of additional cylindrical lenses. As we have seen in previous paragraph these asymmetries can be now even beneficial for our setup. We orient the laser diode in such a way that we get similar asymmetries like in figure 4.21(c). With the help of a collimation aspherical lens and a spherical lens we get the following pump beam parameters Here z_d denotes the distance from waist size to laser diode. In figure 4.22 we see the cross section of the pump beam at the crystal. The parameters in 4.1 are used to simulate the intersection of idler and signal for a bandwidth of $5nm$, which is shown in figure 4.22.

To design the collecting optics we need to determine the divergence of the intersection of idler and signal. To this end we determine the intensity distribution of this

[13] please note that a smaller waist size in vertical plane corresponds to higher divergency of the beam in vertical plane and thus the pump beam is stretched vertically at crystal position, as shown in figure 4.21(b)

[14] as we know this corresponds also to the extraordinary direction in the crystal

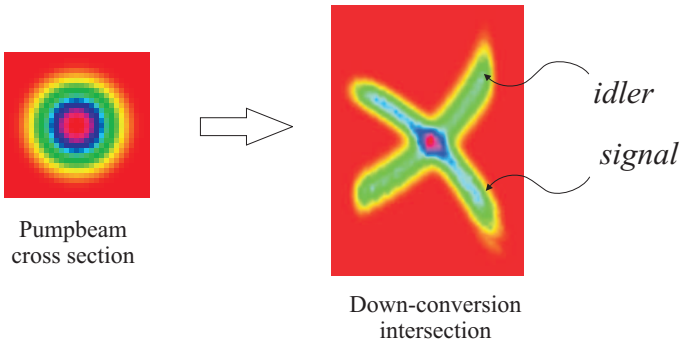

(a) *Circular gaussian pump beam yields a non circular intersection of idler and signal*

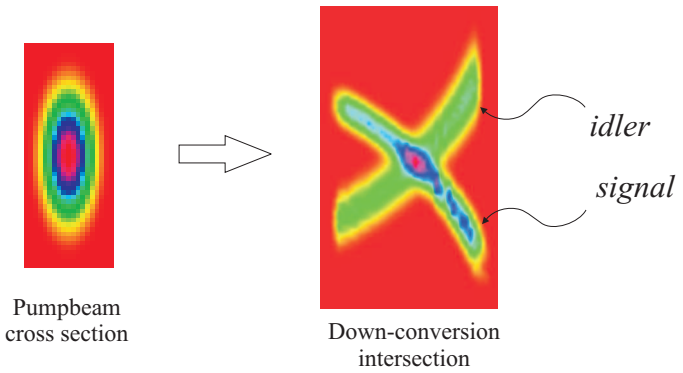

(b) *Elliptical gaussian pump beam (vertical)*

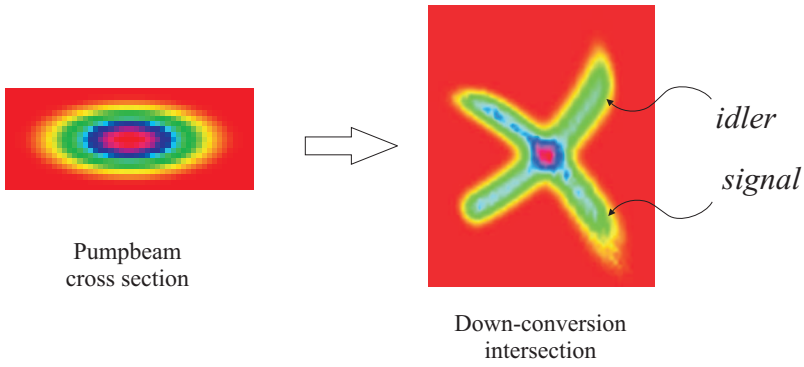

(c) *Elliptical gaussian pump beam (horizontal) yields the most circular intersection shape*

Figure 4.21: *Intersection shape depending on pump beam cross section: an elliptical pump beam shows the most circular intersection of idler and signal, which is necessary for optimal collecting*

Horizontal Plane	w_0	$=$	$96\mu m$
	M^2	$=$	1.96
	z_d	$=$	$0.6m$
Vertical Plane	w_0	$=$	$156\mu m$
	M^2	$=$	1.16
	z_d	$=$	$0.5m$

Table 4.1: *Pump beam parameter*

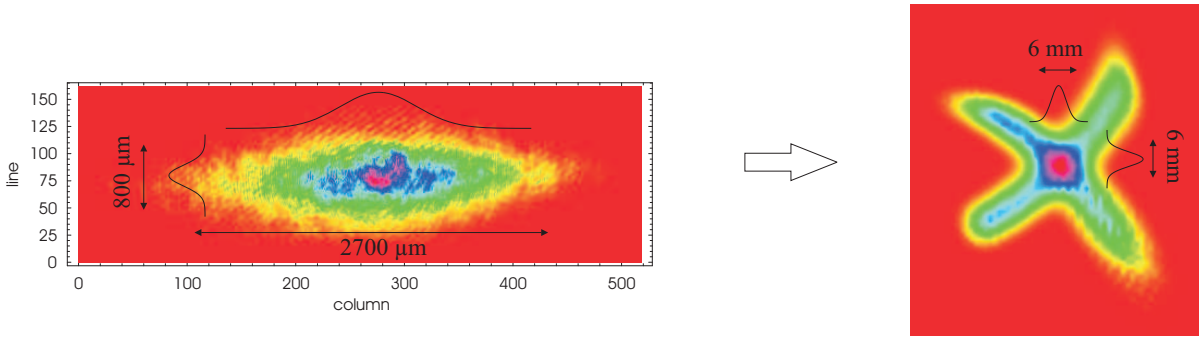

Figure 4.22: *Pump beam cross section at crystal and intersection of idler and signal after* $30cm$

intersection at different positions behind the crystal and fit a gaussian profile to it to obtain its radius. This we do separately in horizontal and vertical plane. In such a way we get the dependency shown figure 4.23. For small distances behind the crystal the intersection is still elliptical, but interestingly, at a distance of 100 mm the shape of the intersection becomes circular. To find the divergence of this circular intersection we make a linear fit to the data shown in figure 4.23. We find for $\theta_{SPDC} \approx 0.28°$. Assuming gaussian optics this corresponds to the waist size of the collecting mode of 50 μm. We use a aspherical lens to transform the mode of the single mode fiber to the calculated mode.

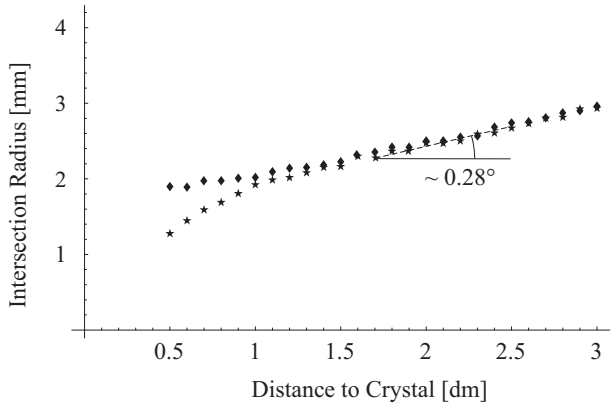

Figure 4.23: *Behavior of intersection with distance: intersection radius of idler and signal in horizontal (♦) and vertical (★) plane*

4.3.2 Results and Problems

For the rough alignment of the source multi-mode fibers, instead of single-mode ones, were used. With them, we observed a slope of 1000 coincident counts per second and mW of pump power. Unfortunately, it was not possible to couple into the single-mode fibers the same amount of photons. We observed 2 orders of magnitudes lower coincident count rates than in the case of multi-mode fibers.

To investigate the coupling process into fibers in more detail we used a ray tracing program, which allowed us to visualize the propagation path of an assemble of rays, while putting various optical components into their path. We used an assemble of down-converted rays[15] calculated with the parameters of table 4.1 according to methods describe in last section. For the ray tracing program only rays were taken which lie in a bandwidth of 5 nm around the degenerate wavelength of 807 nm and have at least an intensity of $1/e^2$ (the maximum intensity corresponds to 1). We place an aspherical lens with focal length of 7.5 mm 20 cm behind crystal[16] and investigate the transformed rays. In horizontal plane the rays are focused to a spatial range of about 80 μm (figure 4.24(a)) and in vertical plane this range is about $50\mu m$ (figure 4.24(b)). This two values can be considered as an approximation of the waist size of down-conversion mode at fiber position.

This result explains why this mode can still be coupled into a multi-mode fiber with a core diameter 50 μm whereas the coupling efficiency into a single-mode fiber with a mode field diameter of 5.2 μm was very poor.

We also asked some companies for a commercial solutions for a lens system to focus these rays down to a diameter of 5.2 μm. No solution was found for our problem.

[15] from one collecting arm

[16] other optical components like $\lambda/2$-Plate, compensation crystal and long pass filter are not taken into account

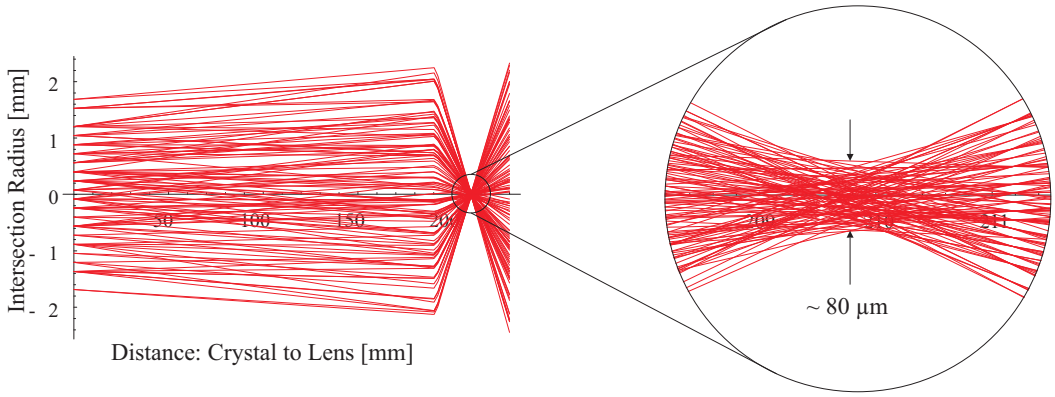

(a) *Horizontal plane: the rays are focused in region of about* $80\mu m$

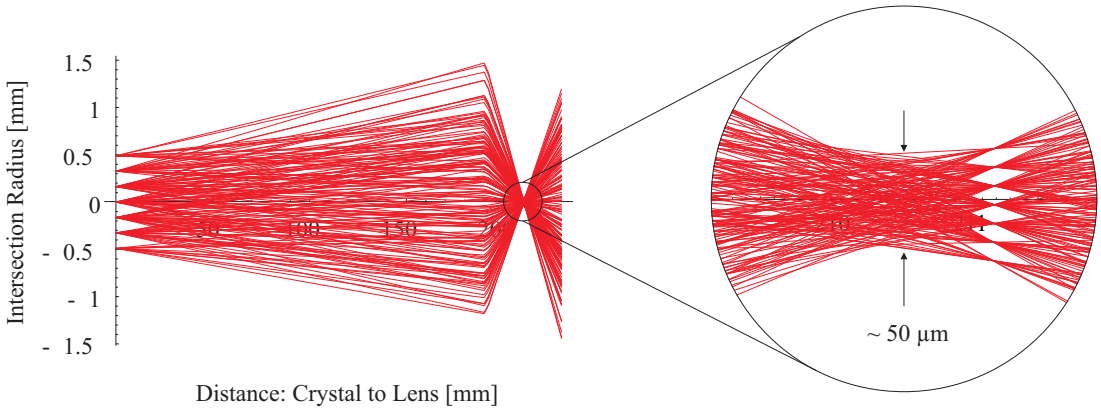

(b) *Vertical plane: the rays are focused in region of about* $50\mu m$

Figure 4.24: *Ray propagation of down-converted rays in horizontal and vertical plane: focusing aspherical lens after* $200mm$

Chapter 5

Outlook

All experiments presented in chapter 4 use SPDC type-II in a non-collinear geometry. In the following outlook we will discuss a new idea for a source, based on SPDC type-I in collinear configuration. It is an improved version of the Kwiat-Source [5], which was shortly presented in 2.3.2. Our setup is expected to be more compact, stable and more efficient than sources presented so far.

After a short overview about the main concept, we will investigate the details of the source. First, we discuss which crystal is the most suitable for this setup. Second, the dependence of the collinearly emitted bandwidth on the pump beam parameters is calculated. Finally I describe the walk-off effects and possible compensations.

5.1 Collinear Setup Type I

In contrast to SPDC type-II, for type-I the polarization entanglement is not given naturally, as the down-converted photons have the same polarization. A very clever idea is presented in [5] and [30] how to prepare a polarization entangled state with SPDC type-I: two identically cut crystals are oriented with their optical axis perpendicular to each other. A 45° polarized pump beam[1] will be equally down-converted in the first and second crystal. We observe photons with orthogonal polarization emitted onto the same cone. These two possible down-conversion processes are coherent with each other, as long as the emitted spatial modes for each of the two crystals are indistinguishable. Collecting the photon pairs we can observe the following state

$$|\psi\rangle = \frac{1}{\sqrt{2}}(|HH\rangle + e^{i\phi}|VV\rangle) \tag{5.1}$$

where the phase (ϕ) between the two photon pairs of the first and second crystal is determined by the crystal thickness. This phase can be adjusted with different design parameters, which one can find in [5].

A modification of this setup promises a more simple source. We choose the pump angle Θ_p that way that two conditions are fulfilled. Firstly, the two idler and signal

[1] with respect to the OA of one of the crystals

photons are emitted collinearly, that means they are emitted in the same direction like the pump beam. This allows for a more simple and robust collection of the photon pairs. Secondly, the wavelength of idler and signal are different and thus can be separated using a *dichroic mirror* into two spatial modes. As all photons of a certain spectral range are emitted in one direction, in contrast to the non-linear case, it is possible to collect all of them.

5.1.1 Choice of crystal

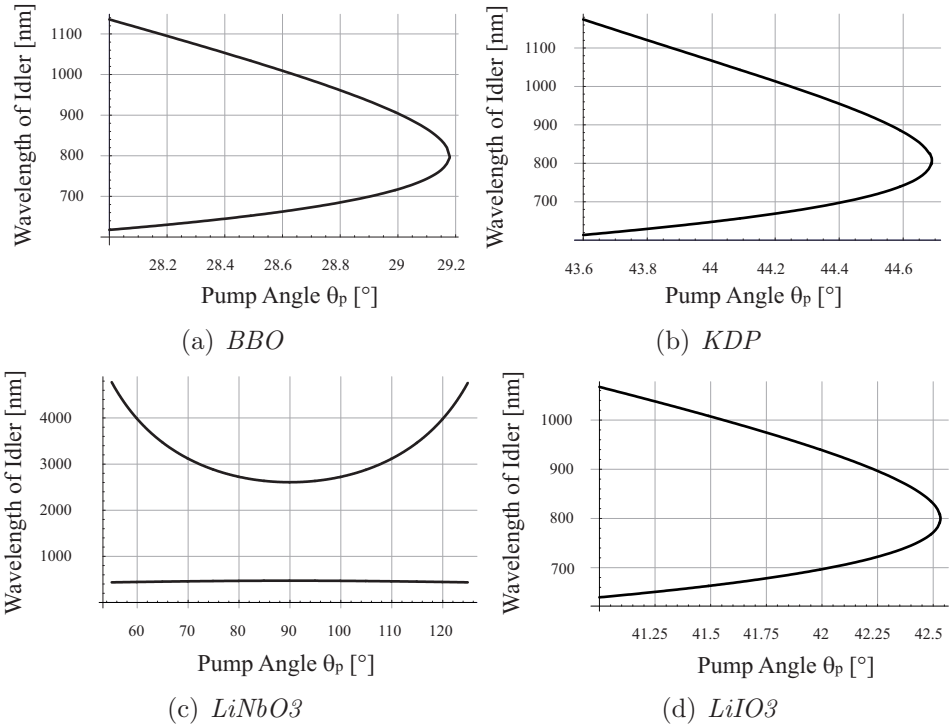

(a) *BBO* (b) *KDP*

(c) *LiNbO3* (d) *LiIO3*

Figure 5.1: *Collinear phase-matching: Pump angle Θ_p versus emitted wavelengthes, idler and signal show the same plot*

In order to find a suitable crystal we compared *BBO*, *KDP* (KD_2PO_4), $LiNbO_3$ and $LiIO_3$, where all of them are uniaxial. First we look at the dependence of the emitted photons versus the pump angle Θ_p for a pump wavelength at 400 nm (figure 5.1). These plots were calculated out of the phase-matching conditions as already discussed in 3.2. We see that in all cases that there exists a pump angle where the emitted photons can be separated. In $LiNbO_3$, however, the emitted wavelength are not acceptable. Out of the remaining crystal we choose the one with the highest *effective nonlinear coefficient*, i.e. Lithium Iodate (LiIO3) (table 5.1). The effective nonlinear coefficient is a measure for the efficiency of the generation of down-converted photons.

Crystal	β-BBO	KDP	LiIO3
Nonlinear coefficient	2.3	0.4	3.68

Table 5.1: *Nonlinear coefficients of crystals of interest*

5.1.2 Emitted wavelength bandwidth

We intended to produce photon pairs which are separated in wavelength, but close to the degenerate case. The reasons are other experimental requirements, for example are the detector efficiencies the highest around 800 nm. As we can see in figure 5.2(a), below a pump angle $\Theta_p = 42.5324°$ these conditions are fulfilled. Considering an angular distribution ($\Delta\Theta_p$) in the pump mode, see also chapter 4.3, the photons will be emitted in a certain bandwidth ($\Delta\lambda_1$ and $\Delta\lambda_2$). A too broad bandwidth lowers the quality of the entanglement. In the scope of this thesis, however, we do not treat these problems, but see [5].

Figure 5.2(b) shows the dependence of the emitted bandwidth versus the pump waist size. According to gaussian optics we determine the angle distribution in a pump beam for various waist sizes, and calculate the bandwidth according figure 5.2(a). As the divergence of a beam with a big waist size is small, pumping with such beam will result a small bandwidth, which is preferable for this experiment.

Because we aim to couple the photons in a single-mode fiber, which provides the TM_{00} mode, we will collect besides the collinear emitted photons also a certain angular distribution, depending on the collecting beam parameters. Due to phase-matching conditions, however, the non-collinear emitted photons do not have the same wavelength. Therefore the collecting optics will also cause a broadening of the spectrum of the collected photons. Further calculation showed that this additional effect is negligible.

5.1.3 Walk-off effect and compensation

In a SPDC type-I process there is no walk-off between the two created photons. In our configuration, however, a walk-off between the photon pairs created in the first and second crystal, due to their orthogonal polarization, can be observed.

The separation angle $\rho(\theta)$ (equation 2.18) of an extraordinary and ordinary beam is used to investigate this effect more in detail. We calculate the following walk-off per crystal thickness in a LiIO3 crystal.

Wavelength	*Walk-Off*
UV	$68\mu m/1mm$
IR	$65\mu m/1mm$

Table 5.2: *Transversal Walk-Off for LiIO3 per* $1mm$ *crystal thickness: depending on the wavelength the extraordinary beam will be shifted in respect to the ordinary beam*

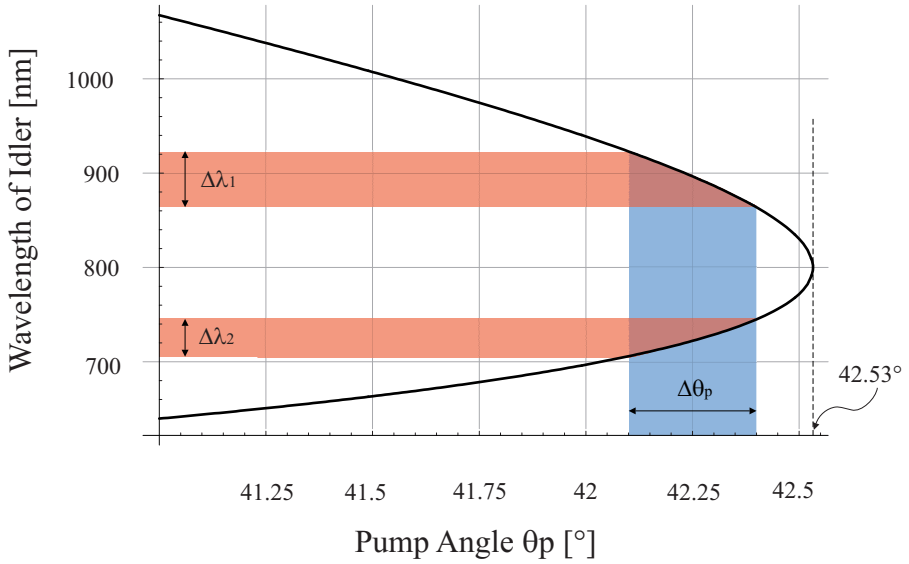

(a) *Collinear SPDC type-I (LiIO3): for a pump angle $\theta_p = 42.53°$ we have the degenerate case; working point is chosen slightly smaller; due to angle distribution in pump beam $\Delta\theta_p$ we have a wavelength distribution in down-converted photons ($\Delta\lambda_1$, $\Delta\lambda_2$)*

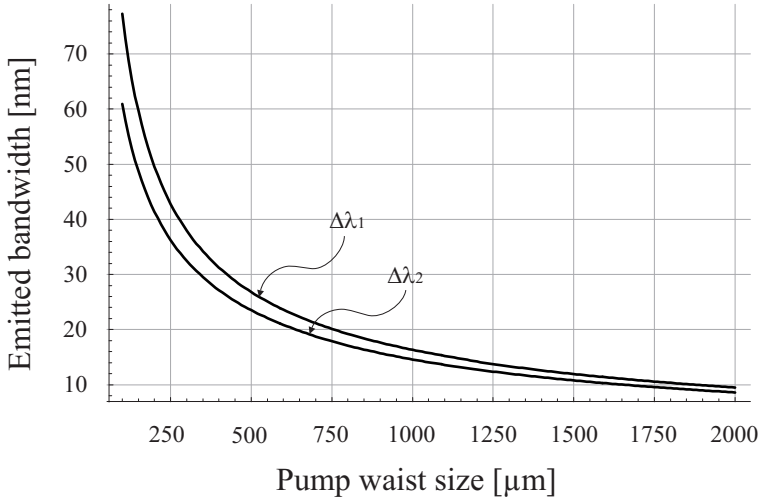

(b) *Bandwidth of down-converted photons versus pump beam waist size*

Figure 5.2: *Emitted wavelength bandwidth depending on pump waist size*

Using the values out of table 5.2 we calculate the walk-off[2] shown in figure 5.3(a). The pump beam, which has an extraordinary polarization, is diverted passing the first crystal. The down-converted photons, with an ordinary polarization, will form therefore an elliptically shaped beam. In the second crystal this beam show an extraordinary polarization, due to the crossed configuration. Thus it is diverted like the pump beam.

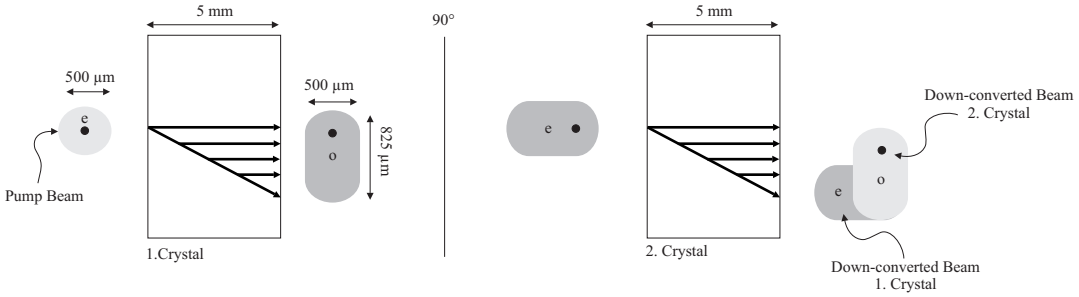

(a) *Transversal Walk-Off for an example: pump beam radius* $500\mu m$*; crystal thickness* $5mm$

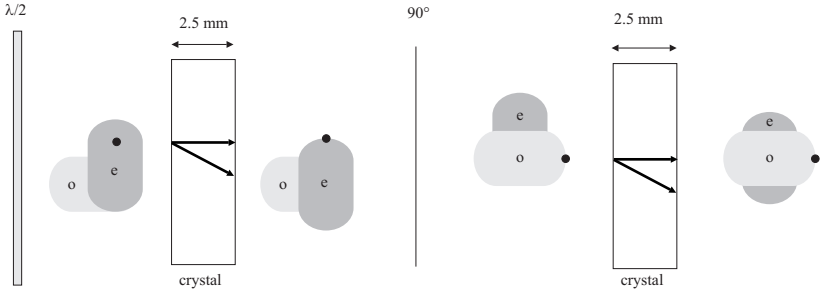

(b) *The compensation is realized with also two crossed crystals which are half as thick as the main crystals*

Figure 5.3: *Transversal Walk-Off and compensation for a specific example; the black dot marks the center of the pump beam*

Similar in the case of SPDC type-II we compensate the walk-off with a $\lambda/2$-Plate and two crossed crystals with the half thickness with respect to the main crystals.

5.1.4 Conclusion

We presented the main idea of a new source for polarization entangled photon pairs and investigated the details, like the choice of the crystal, the collected bandwidth of emitted photons and transversal walk-off.

A possibility how one could realize such a setup in a very compact and stabile way is shown in figure 5.4. The pump beam is provided from a fiber coupled laser diode. It is transformed with a aspherical lens to a collimated beam with a almost arbitrary big diameter. The down-converted photons are generated in a crystal configuration, consisting out of the two optically contacted, perpendicularly oriented crystals. The walk-off is compensated by the combination of a $\lambda/2$-plate and the compensation

[2]an example is investigated where the crystal is 5 mm thick and the pump beam has a diameter of 500 μm

crystal. To filter out the pump beam we use a long pass filter. The collinear down-conversion emission has the same diameter as the pump beam and is collected into a single-mode fiber-coupled wavelength division multiplexer to separate the photon pairs. The big diameter of the pump beam allows for a narrow spectral bandwidth of the down-conversion which is necessary for achieving high quality of entanglement. Further the collimation of the pump beam and the collecting mode allows for a compact and robust design.

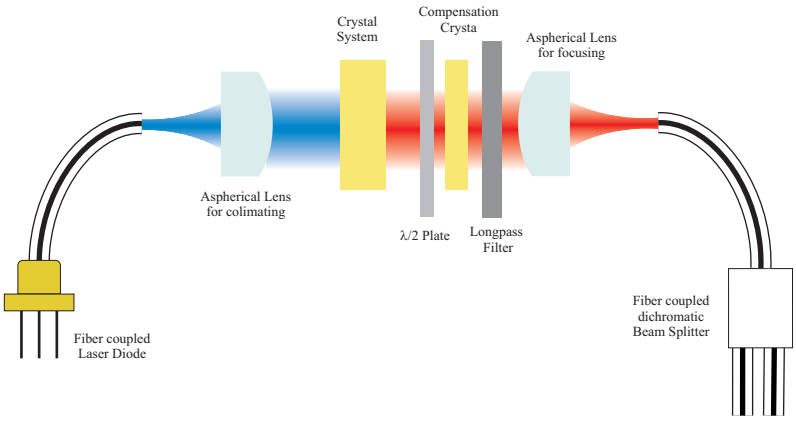

Figure 5.4: *Proposal for a collinear SPDC type-I with crossed crystals: The main point of this setup is to chose a collimated pump and collecting mode, this results a narrow bandwidth of the down-converted photons and allows to move very near from both sides to the crystal; the use of fibre coupled laser diode and dichromatic beam splitters allows a more compact and stable source*

Many issues concerning the implementation of this idea still need to be investigated more carefully like the dispersion effects occurring in down-conversion crystal. For further details see also [5] and [30].

Appendix A

Crystal Properties

A.1 β-BBO

In the experimental part of this thesis we used a β-Barium Borate ($\beta - BaB_2O_4$), also called BBO crystal. This crystal is an uniaxial negative crystal, i.e. $n_e < n_o$. The values for n_e and n_o are given by the corresponding Sellmeier equations [24]

$$n_o^2(\lambda) = 2.7359 + \frac{0.01878}{\lambda^2 - 0.001822} - 0.01354\lambda^2 \tag{A.1}$$

$$n_e^2(\lambda) = 2.3753 + \frac{0.01224}{\lambda^2 - 0.001667} - 0.01516\lambda^2 \tag{A.2}$$

where λ is given in μm.

The effective nonlinear coefficient is defined the following way

$$d_{eff} = d_{31}\sin\theta + (d_{11}\sin 3\phi - d_{22}\cos 3\phi)\cos\theta \tag{A.3}$$

for phase-matching type-I and

$$d_{eff} = (d_{11}\sin 3\phi - d_{22}\cos 3\phi)\cos^2\theta \tag{A.4}$$

for phase-matching type-II. With the following parameters

$$\begin{aligned} d_{11} &= 5.8 d_{36}(KDP) \\ d_{22} &< 0.05 d_{11} \\ d_{31} &= 0.05 d_{11} \end{aligned} \tag{A.5}$$

where ϕ and θ are the polar and azimuthal angles to the optical axis.

For the experiment it was calculated for phase-matching type-II. By setting $\theta = \Theta_p = 42.84°$ we get a maximum for the effective nonlinear coefficient at $\phi = 30.95°$, namely $d_{eff} = 1.37[pm/V]$. This angle will be used to cut the crystal in such a way that we gain the maximal down-conversion efficiency.

The nonlinear coefficients are summarized in table A.1.

	Type-I	*Type-II*
Pump angle Θ_p	$29°$	$42.84°$
Nonlinear Coefficient d_{eff}	$2.3pm/V$	$1.37pm/V$

Table A.1: *BBO nonlinear coefficients: type-I and -II*

The crystal edges was anti reflection coated for IR and UV.
Other useful properties for the design are listed in table A.2.

Density	$3.85g/cm^3$
Absorbtion Coefficient	$< 0.1\%/cm$ @$1064nm$
Transparency Range	$189 - 3500nm$
Damage Threshold	$1GW/cm^2(10ns)$ @$532nm$

Table A.2: *BBO crystal properties*

A.2 LiIO3

Lithium Iodate ($LiIO_3$) we proposed to use in the setup introduced in chapter 5.1. The used Sellmeier equations are the following [31]

$$n_o^2 = 3.415716 + \frac{0.047031}{\lambda^2 - 0.035306} - 0.008801\lambda^2 \tag{A.6}$$

$$n_e^2 = 2.918692 + \frac{0.035145}{\lambda^2 - 0.028224} - 0.00364\lambda^2 \tag{A.7}$$

Lithium Iodate is a uniaxial negative crystal. We calculate a maximum effective nonlinear coefficient $d_{eff} = 3.68pm/V$, for phase-matching type-I.
Other proper of interest are listed in the next table [31].

Density	$4.5g/cm^3$
Absorbtion Coefficient	$< 0.5\%/cm$ @$1064nm$
Transparency Range	$300 - 5000nm$
Damage Threshold	$0.25GW/cm^2(20ns)$ @$1064nm$

Table A.3: $LiLO_3$ *crystal properties*

A.3 KDP

Potassium Dihydrogen Phosphate (KD_2PO_4), also called KDP, is an uniaxial negative crystal, with the following Sellmeier equations [31]

$$n_o^2 = 2.259276 + \frac{0.01008956}{\lambda^2 - 0.012942625} + \frac{13.00522\lambda^2}{\lambda^2 - 400} \tag{A.8}$$

$$n_e^2 = 2.132668 + \frac{0.008637494}{\lambda^2 - 0.012281043} + \frac{3.2279924\lambda^2}{\lambda^2 - 400} \tag{A.9}$$

For the nonlinear coefficient we calculate $0.4pm/V$.

Density	$2.24g/cm^3$
Absorbtion Coefficient	$< 7\%/cm$
Transparency Range	$200 - 1500nm$
Damage Threshold	$> 5GW/cm^2$ @$1064nm$

Table A.4: *KDP crystal properties*

A.4 LiNbO3

The used Sellmeier equations for Lithium Niobate Crystal ($LiNbO_3$) are the following

$$n_o^2 = 4.9048 + \frac{0.11768}{\lambda^2 - 0.04750} - 0.027169\lambda^2 \tag{A.10}$$

$$n_e^2 = 4.5820 + \frac{0.099169}{\lambda^2 - 0.04443} - 0.02195\lambda^2 \tag{A.11}$$

Bibliography

[1] A. Einstein, B. Podolsky, and N. Rosen. Can quantum-mechanical desciption of physical reality be considered complete? *Phys. Rev.*, 47(777), 1935.

[2] C. H. Bennet and S. J. Wiesner. Communication via one- and two-particle operators on einstein-podolsky-rosen states. *Phys. Rev. Lett.*, 69(2881), 1992.

[3] C. H. Bennet, G. Brassard, C. Crépeau, R. Jozsa, A. Peres, and W. K. Wootters. Teleporting an unknown quantum state via dual classical and einstein-podolsky-rosen channels. *Phys. Rev. Lett.*, 70(1895), March 1993.

[4] A. K. Ekert. Quantum cryptography based on bell's theorem. *Phys. Rev. Lett.*, 67(661), 1991.

[5] P. G. Kwiat, E. Waks, A. G. White, I. Appelbaum, and P. H. Eberhard. Ultrabright source of polarization-entangled photons. *Phys. Rev. A*, 60(2), 1998.

[6] H. Weinfurter M. Oberparleiter. Cavity-enhanced generation of polarization-entangled photon pairs. *Opt. Com.*, 183(133-137), 2000.

[7] S. Tanzilli, H. De Riedmatten, W. Tittel, H. Zbinden, P. Baldi, M. De Micheli, D.B. Ostrowsky, and N. Gisin. Highly efficient photon-pair source using a periodically poled lithium niobate waveguide. *Electronics Letters*, 2001.

[8] J. S. Bell. On the einstein-podolsky-rosen paradox. *Physics*, 1, 1964.

[9] J. F. Clauser, M. A. Horne, A. Shimony, and R . A. Holt. Proposed experiment to test local hidden-varialbe theories. *Phys. Rev. Lett.*, 23(880), 1969.

[10] A. Aspect, P. Grangier, and G. Roger. Experimental realization of einstein-podolsky-rosen-bohm gedankenexperiment: A new violation of bell's inequalities. *Phys. Rev. Lett.*, 49(2), December 1981.

[11] K. Mattle, H. Weinfurter, P. G. Kwiat, and A. Zeilinger. Dense coding in experimental quantum communication. *Phys. Rev. Lett.*, 76(4656), 1996.

[12] D. Bouwmeester, J. Pan, K. Mattle, M. Eibel, H. Weinfurter, and A. Zeilinger. Experimental quantum teleportation. *Nature*, 390(575), December 1997.

[13] S. Wiesner. Conjugate coding. *Sigact News*, 15(78), 1983.

[14] C. H. Bennet and G. Brassard. Quantum cryptography: Public key distribution and coin tossing. *Proceedings of IEEE International Conference on Computers, Systems and Signal Processing, Bangalore, India,*, 1984.

[15] P. G. Kwiat, K. Mattle, H. Weinfurter, A. Zeilinger, A. V. Sergienko, and Y Shih. New high-intensity source of polarization-entangled photon pairs. *Phys. Rev. Lett.*, 75(4337), 1995.

[16] Markus Oberparleiter. *Effiziente Erzeugung Verschraenkter Photonenpaare*. PhD thesis, Ludwig-Maximilians-Universitaet Muenchen, 2002.

[17] Bahaa E. A. Saleh and Malvin Carl Teich. *Fundamentals of Photonics*. 1994.

[18] Ammon Yariv. *Optical Electronics in ModernCommunication*. Oxfort University Press, fifth edition, 1997.

[19] Thomas F. Johnston. Beam propagation (m^2) mesurement made as easy as it gets: the four-cut method. *Applied Optics*, 37(21), July 1998.

[20] V. G. Dmitriev, G. G. Gurzadyan, and D. N. Nikogosyan. *Handbook of Nonlinear Optical Crystals*. Springer, 1997.

[21] Ch. Kurtsiefer, M. Oberparleiter, and H. Wienfurter. Hight-efficiency entangled photon pair collection in type-ii parametric flourescence. *Phys. Rev. A*, 64(023802), July 2001.

[22] G. P. Agrawal. *Fiber-Optic Communication Systems*. 2002.

[23] P. Trojek, Ch. Schmid, M. Bourennane, Ch. Kurtsiefer, and H. Weinfurter. Compact source of polarization-entangled photon pairs. *Optical Society of America*, 270.0270(230.6080), 2003.

[24] Inc. Foctek Photonics. *http://www.foctek.net*.

[25] S. Nakamura, G. Fasol, and S. J. Pearton. *The Blue Laser Diode: The Complete Story*. Springer Verlag, 2000.

[26] Grintech gmbh, gradient index optics technology. *http://www.grintech.de*.

[27] D. F. V. James, P. G. Kwiat, W. J. Munro, and A. G. White. Measurement of qubits. *Phys. Rev. A*, 64(052312), 2001.

[28] D. N. Klyshko. Effect of focusing on photon correlation in parametric ligth scattering. *Sov. Phys. JETP*, 67(6), 1988.

[29] C. H. Monken, P. H. Souto Ribeiro, and S. Padua. Optimizing the photon pair collection efficiency: A setp towards a loophole-free bell's inequalitoes experiment. *Phys. Rev. A*, 57(4), 1997.

[30] A. G. White, D. F. V. James, P. H. Eberhard, and P. G. Kwiat. Nonmaximally entangled states: Production, characterization, and utilization. *Phys. Rev. Lett.*, 83(16), 1999.

[31] Inc. Fujian CASTECH Crsytals. *http://www.castech.com.*